



**HAL**  
open science

## Automated fibre placement process for a new hybrid material: A numerical tool for predicting an efficient heating law

Omar Baho, Gilles Ausias, Yves Grohens, Marco Barile, Leonardo Lecce, Julien Férec

► **To cite this version:**

Omar Baho, Gilles Ausias, Yves Grohens, Marco Barile, Leonardo Lecce, et al.. Automated fibre placement process for a new hybrid material: A numerical tool for predicting an efficient heating law. Composites Part A: Applied Science and Manufacturing, 2021, 144, pp.106360. 10.1016/j.compositesa.2021.106360 . hal-03157138

**HAL Id: hal-03157138**

**<https://hal.science/hal-03157138>**

Submitted on 10 Mar 2023

**HAL** is a multi-disciplinary open access archive for the deposit and dissemination of scientific research documents, whether they are published or not. The documents may come from teaching and research institutions in France or abroad, or from public or private research centers.

L'archive ouverte pluridisciplinaire **HAL**, est destinée au dépôt et à la diffusion de documents scientifiques de niveau recherche, publiés ou non, émanant des établissements d'enseignement et de recherche français ou étrangers, des laboratoires publics ou privés.



Distributed under a Creative Commons Attribution - NonCommercial 4.0 International License

# Automated fibre placement process for a new hybrid material: A numerical tool for predicting an efficient heating law

Omar Baho<sup>a</sup>, Gilles Ausias<sup>a</sup>, Yves Grohens<sup>a</sup>, Marco Barile<sup>b</sup>, Leonardo Lecce<sup>b</sup>, Julien Férec<sup>a,\*</sup>

<sup>a</sup>*Univ. Bretagne Sud, UMR CNRS 6027, IRDL, F-56100 Lorient, France*

<sup>b</sup>*NOVOTECH Aerospace Advanced Technology, Naples, Italy*

---

## Abstract

An innovative hybrid thermoplastic manufacturing process has been investigated, which consists in carbon fibres reinforced poly(ether-ether-ketone) (PEEK) prepreg sandwiched between two amorphous polyetherimide (PEI) films. By using a laser-assisted automated fibre placement (AFP), a laminate is produced by the deposition of hybrid prepreg tapes, layer-by-layer without using autoclave. The temperature history control is required to ensure good consolidation throughout the part. This depends on the optical behaviour of the hybrid material, which is also subjected to the influence of process parameters. Before determining the optical properties of the new hybrid material, the correlation between these process parameters has been established based on the interaction of laser spot with PEI film and PEEK/carbon fibres tape. Then, the thermal distribution in the laminate is obtained via an optico-thermal model and

---

\*Corresponding author

*Email address:* [julien.ferec@univ-ubs.fr](mailto:julien.ferec@univ-ubs.fr) (Julien Férec)

validated with experimental results. Finally, a heating law for the AFP process is established using iterative numerical simulations.

*Keywords:* Laser-assisted automated fibre placement, New hybrid thermoplastic composite, Optico-thermal analysis, Heating law

---

## 1. Introduction

The interest of thermoplastic composite materials by using an additive manufacturing (AM) out of autoclave is in continuous evolution due to their promised benefits in terms of work time and costs [1, 2, 3]. In this regard, a new hybrid thermoplastic composite material has been developed to answer  
5 to the needs for reduced weight and consequently reduced fuel consumptions and emissions of aircrafts, as well as reduced manufacturing and operational costs, since it does not require the use of an autoclave curing phase. Indeed, the proposed high-performing material is based on a commercial semi-crystalline PEEK-carbon fibre prepreg (called APC-2) embedded in  
10 amorphous (PEI) film. Therefore, this hybrid material allows to manufacture advanced composite aerostructures by fast and automated processes, such as automated fibre placement (AFP) machines equipped with high-power laser-diodes, at a temperature just above the glass transition temperature ( $T_g$ ) of the amorphous layer and lower than the fusion temperature ( $T_f$ )  
15 of the semi-crystalline APC-2 in order to preserve its optimal degree of crystallinity [3, 4, 5, 6].

The present study aims to improve the productivity of automated laser fibre placement through hybrid material analysis which involve three steps such as heating, melting and solidification to produce good finished

20 parts [7, 8, 9, 10, 11]. To control these steps, a complete comprehension of the laser distribution on the heated surfaces and the thermal history of laminate during process is required [9, 12]. Generally, the temperature history control on the tape placement needs to know the energy distribution on the surface and through the thickness of the composite [7]. In the case  
25 of the thermoplastic composite tape made with continuous unidirectional fibres, near-infrared (NIR) diode lasers are promising sources to melt the thermoplastic and are able to provide higher heat fluxes in near instantaneous response time [13, 14, 15, 16]. The laser interaction with thermoplastic composites can be estimated using a ray-tracing method [13, 16, 7]. For  
30 instance, Groupe [7] investigated the energy input distribution on the carbon/PPS unidirectional surfaces generated by a laser optic source. A 2D ray-tracing method including the reflectance phenomena was developed to calculate the flux distribution in the substrate and incoming tapes. Stokes-Griffin and Compston [9] evaluated the heat input on APC-2 material  
35 using a 3D ray-tracing model developed in CAD. Dolo [13] and Baho et al. [17] developed a 2D ray-tracing method by taking into account the reflection phenomena under the roller deformation and the effects of the AFP process parameters. The data from these ray-tracing models are then used as heat input distribution for thermal models in order to determine the temperature  
40 distribution in the material. A knowledge of this distribution helps to establish relevant heating laws in terms of speed and laser power input, and to avoid excessive high temperatures, which can degrade the polymer [4]. Kollmannsberger et al. [18] conducted a more realistic thermal model by considering thermal contact resistances and non-uniform laser heat inputs.

45 Analytical solutions have been presented in [19, 20]. For instance, Weiler et al. [19] developed a simplified analytical model to control the temperature distributions and the surface temperature of the substrate. Francesco et al. [20] proposed a semi-empirical thermal model which is used to keep constant the nip-point temperature in terms of laser power and layup speed. 50 However, the use of numerical models is still the best method to model the AFP process without reducing the number of assumptions considered in analytical solutions.

In the case of the thermoplastic composite, the optico-thermal models previously developed on the AFP treat standard prepreg tapes. Generally, 55 these ribbons consist of a thermoplastic matrix reinforced with carbon fibres. The required temperature applied during the AFP process to join two parts by fusion and consolidation depends on the type of thermoplastic matrix. For amorphous materials, the required temperature will be higher than the transition temperature while the one for semi-crystalline matrices 60 will be above the melting temperature [21, 22]. The aim of this work is to characterize and analyze the manufacturing process of a new hybrid thermoplastic composite (HTPC) combining an amorphous material and semi-crystalline reinforced with carbon fibres.

In this paper, the optical and thermal behaviours of a HTPC under 65 the effects of the AFP head parameters are modelled. The HTPC tape is produced by the combination of the aromatic polymer composite (APC-2) embedded in two PEI films. In AFP process, the laminate is produced layer by layer in which the incoming tape and substrate are consolidated by heating their respective surfaces and applying a pressure load. The most

70 sensitive process parameters to achieve a good consolidation between the  
different layers without degrading the thermoplastic are the temperature  
in the consolidation area (i.e., nip-point process), the layup speed and the  
roller compaction force. These parameters need to be well controlled so  
that they stay within a specific optimum parameter range. Furthermore,  
75 the laser-heating system is chosen as the heat source in the simulations. In  
particular, the use of lasers as a heating source puts very high requirements  
on the process control system. For this reason, a ray-tracing procedure is  
developed in MatLab software, based on geometric optics to determine the  
laser heat-flux distribution on the composite. Additionally, the ray-tracing  
80 method requires to know the thermal radiative properties of HTPC, which  
are characterised and evaluated in terms of the angle of incidence, the  
wavelength, the head tilt and the roller deformation. After computing the  
radiative source term, these data are used to calculate the temperature  
distribution on the surface and through the thickness of the composite by  
85 performing finite element analyses with the commercial software Abaqus.

## 2. Thermo-optical properties

This section deals with some optical properties and thermal  
characterisations of the HTPC, which represents the main key to investigate  
the interaction between the laser beam and the laminate during the AFP  
90 process.

### 2.1. *The new hybrid material*

Fig. 1 shows the HTPC which consists of two PEI films overlying  
PEEK/carbon fibres material. PEI is an amorphous polymer with a reported

$T_g = 217^\circ C$ , while PEEK is a semi-crystalline polymer with  $T_g = 143^\circ C$  and a  
95 melting temperature  $T_m = 343^\circ C$ . The addition of amorphous PEI film to the  
commercial PEEK/carbon fibres (APC-2) aims to improve the processability  
of crystalline PEEK [23, 24, 25]. The hybrid material is obtained by heating  
both a commercial APC-2 and two PEI films over the melting temperature of  
PEEK. The consolidation step is carried out by a continuous process under  
100 controlled parameters (i.e., temperature distribution, pressure, time, feeding  
speed rate) [23]. The initial thicknesses of the PEI and PEEK/carbon fibres  
films before this consolidation step are  $t_{PEI} = 50 \mu m$  and  $t_{APC-2} = 127 \mu m$ ,  
respectively. After consolidation of three layers constituting the hybrid  
material, the thickness obtained is greater than the sum of the nominal  
105 thicknesses (Fig. 1). This can be justified by the morphological change of  
the material occurred during the continuous material production process.  
Specifically, the mixing between PEEK and PEI phases promotes the growth  
of the APC-2 / PEI interface, which is caused by a decrease in PEEK  
crystallinity. This has also been observed by Alvaredo-Atienza et al. [26].  
110 Finally, the HTPC is split to a width of  $6.35 mm$  and placed on bobbins for  
feeding the AFP machine.

## 2.2. Optical properties

One of the most important requirement for accurately controlling  
laser-material interaction is the optical properties as a function of the laser  
115 wavelength and incident angle such as complex refractive index, reflection and  
penetration depth of laser irradiation. Generally, when a laser beam strikes a  
material surface, part of its energy is reflected, another absorbed and the rest  
can be transmitted through material. The amounts of absorption, reflection

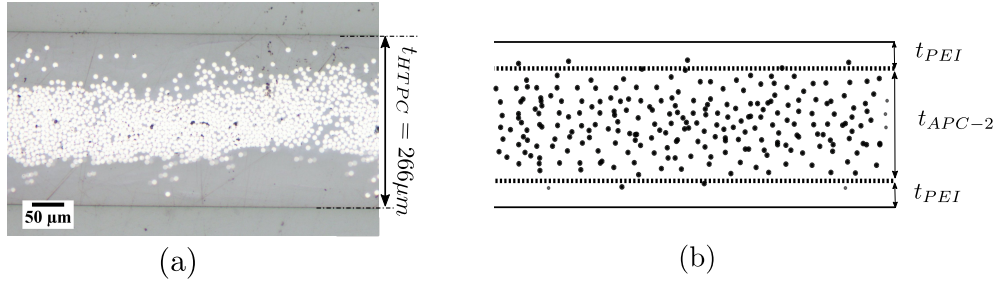


Fig. 1: Cross-section of the hybrid thermoplastic composite (HTPC)

(a): SEM observation; (b): Schematic representation

and transmission depend on the wavelength  $\lambda$  of the incident beam and  
 120 the fiber orientations [27, 28]. The spot size, including the laser intensity  
 distribution and profile, is another parameter that should be considered  
 especially in the case of the laser divergence.

For the HTPC material, three materials are in interaction with the laser  
 beam as depicted in Fig. 2.

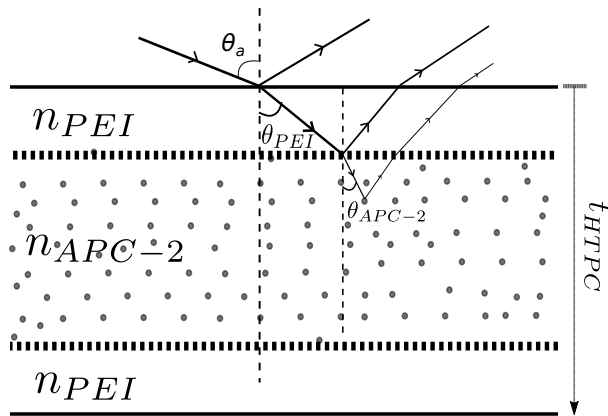


Fig. 2: Interaction of light with HTPC

125 The optical properties of the hybrid material may be deduced from the

complex index of refraction of its constituents  $N_{APC-2}(\lambda) = n_{APC-2}(\lambda) - ik_{APC-2}(\lambda)$  and  $N_{PEI}(\lambda) = n_{PEI}(\lambda) - ik_{PEI}(\lambda)$ , where  $n$  the real part and  $k$  is the extinction coefficient. This allows to determine the absorption  $\alpha$  of the laser irradiation by the material as a function of the wavelength such as

130  $\alpha = 4\pi k/\lambda$ .

Measurements of reflectance  $R_{PEI}$  and transmittance  $T_{PEI}$  are conducted on the PEI film sample by using a spectrometer with an integrating sphere working from ultraviolet to NIR. Therefore, the complex refractive index is obtained from the following analytical expression [29]

$$n_{PEI}(\lambda) = \frac{1 + R(\lambda)}{1 - R(\lambda)} \sqrt{4 \frac{R(\lambda)}{[1 - R(\lambda)]^2} - [k_{PEI}(\lambda)]^2} \quad (1)$$

$$k_{PEI}(\lambda) = \frac{\lambda}{4\pi t_{PEI}} \log \left( \frac{R(\lambda) T_{PEI}(\lambda)}{R_{PEI}(\lambda) - T_{PEI}(\lambda)} \right) \quad (2)$$

135 where  $t_{PEI}$  is the thickness of the film and  $R$  is the corrected reflectance. The refractive indices obtained from Eqs. 1 and 2 for PEI and PEEK are found to be independent on the wavelengths emitted by the laser optics of the AFP machine ( $800 < \lambda < 1100 \text{ nm}$ ) which is 1.6 for PEI and 1.7 for PEEK, respectively. Furthermore, the extinction coefficients are almost zero

140 in this wavelength range, which means that the PEI and the PEEK materials are not directly heated by absorption of laser irradiation.

The refractive index of APC-2 has been computed based on the rule of mixtures (Eq. 3) and the result is reported in Fig. 3.

$$\begin{aligned}
n_{APC-2} &= n_f v_f + n_{PEEK} v_{PEEK} \\
k_{APC-2} &= k_f v_f + k_{PEEK} v_{PEEK}
\end{aligned}
\tag{3}$$

where  $v_{PEEK} = 61\%$  and  $v_f = 39\%$  are the volume fraction of the PEEK  
145 matrix and carbon fibres, respectively.  $n_f$  is the real part of the complex  
refractive index of the carbon fibres and  $k_f$  is its imaginary part. The values  
of these indices as a function of the wavelength are given by Borghesi and  
Guizzetti [30]. To ensure that the hybrid material is opaque at wavelengths  
between 500 and 1100  $nm$ , a transmission spectrum is performed with a  
150 Bruker Vertex v70 IRTF. The obtained results show that the maximum value  
of the transmission coefficient as a function of the wavelength does not exceed  
0.1%. In addition, the APC-2 is the material which absorbs energy according  
to its refractive index, as shown in Fig. 3, and given that the extinction  
coefficient of PEI is zero. The reflectance for the HTPC and PEI is calculated  
155 from the Snell's law and Fresnel equations. Then, the Fresnel coefficients (s  
and p-polarisation) are obtained as a function of the incidence angle  $\theta_a$  [31].  
Fig. 4 depicts the total reflectance for the HTPC, PEI and APC-2 samples  
obtained from s-polarised and p-polarised lights. It is found that the APC-2  
reflectance is most important in light of p-polarisation (see Fig. 5), which  
160 means that the light will behave differently depending on the polarisation  
type. Therefore, a comparative inspection of HTPC reflectance and that  
reported for APC-2 [9] indicates that the reflectance of the HTPC is slightly  
higher than that of the APC-2, although the PEI material is semi-transparent  
and its extinction coefficient is roughly zero. This is because the laser beam  
165 intensity  $I(\lambda, t_{HTPC} = 0)$  is initially attenuated by the reflection at the

air/PEI interface. Hence, the real irradiation intensity reaching the opaque portion of the hybrid material (i.e., APC-2) is  $(1 - R(\theta_a))I(\lambda, 0)$ , where  $R(\theta_a)$  is the reflectance of the HTPC material. The attenuation of crossing intensity within the HTPC can be described by the Bouguer's law

$$I(\lambda, t) = (1 - R(\theta_a))I(\lambda, t_{PEI})e^{-\alpha(\lambda)t_{HTPC}} \quad (4)$$

170 Therefore, the attenuation factor through the HTPC of thickness  $t_{HTPC}$  is defined by the ratio  $\eta = I(\lambda, t_{HTPC})/I(\lambda, t_{PEI})$ . From the refractive index of PEI film and data in Fig. 3, the attenuation factor  $\eta$  is calculated using Eq. 4. Fig. 6 shows the penetration depth of irradiation in the HTPC for  $\lambda = 980 \text{ nm}$ . For  $t_{HTPC} \geq 61.3 \text{ }\mu\text{m}$ , the irradiation is almost completely  
 175 absorbed in the APC-2. It is important to note that the penetration depth of APC-2 is  $0.3 \text{ }\mu\text{m}$  given that  $61 \text{ }\mu\text{m}$  represents the average thickness of PEI film after joining the PEI film and the APC-2 material. As indicated in Fig. 6, the depth of penetration also depends on the incident angle  $\theta_a$ . For the AFP process, the incident angle is less than  $\theta_a \leq 60^\circ$ , which means that  
 180 the attenuation factor does not exceed 0.75.

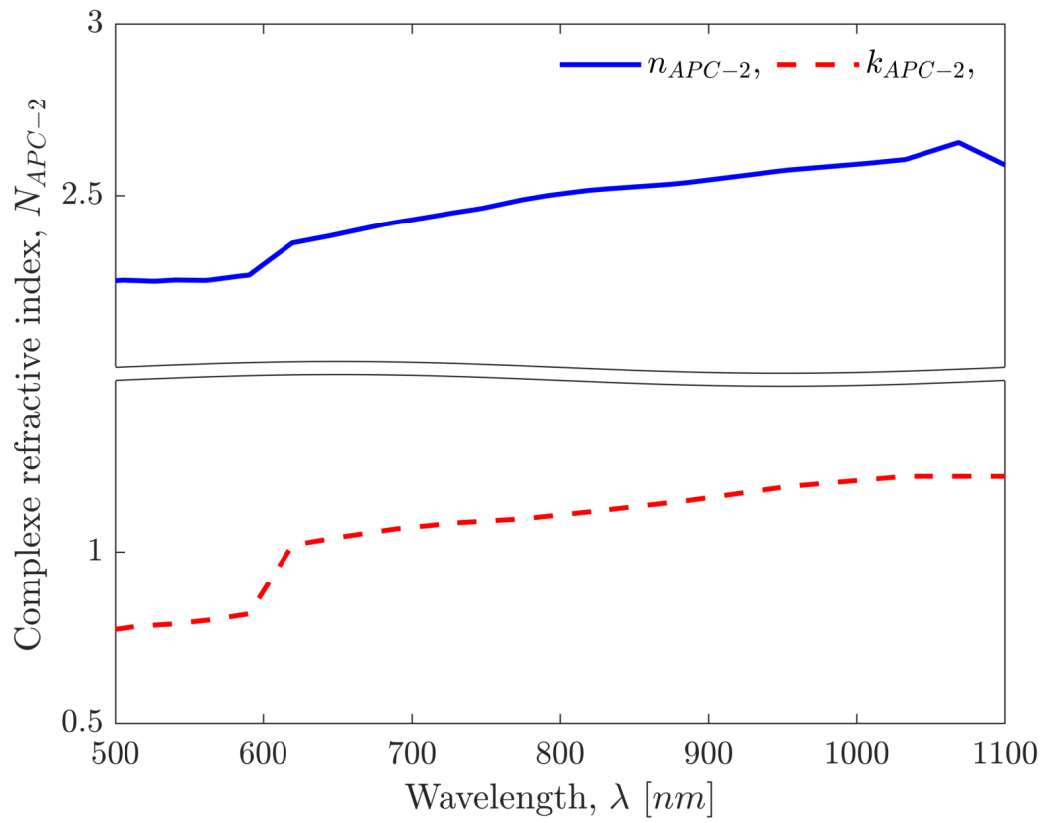


Fig. 3: Complex refractive index for APC-2

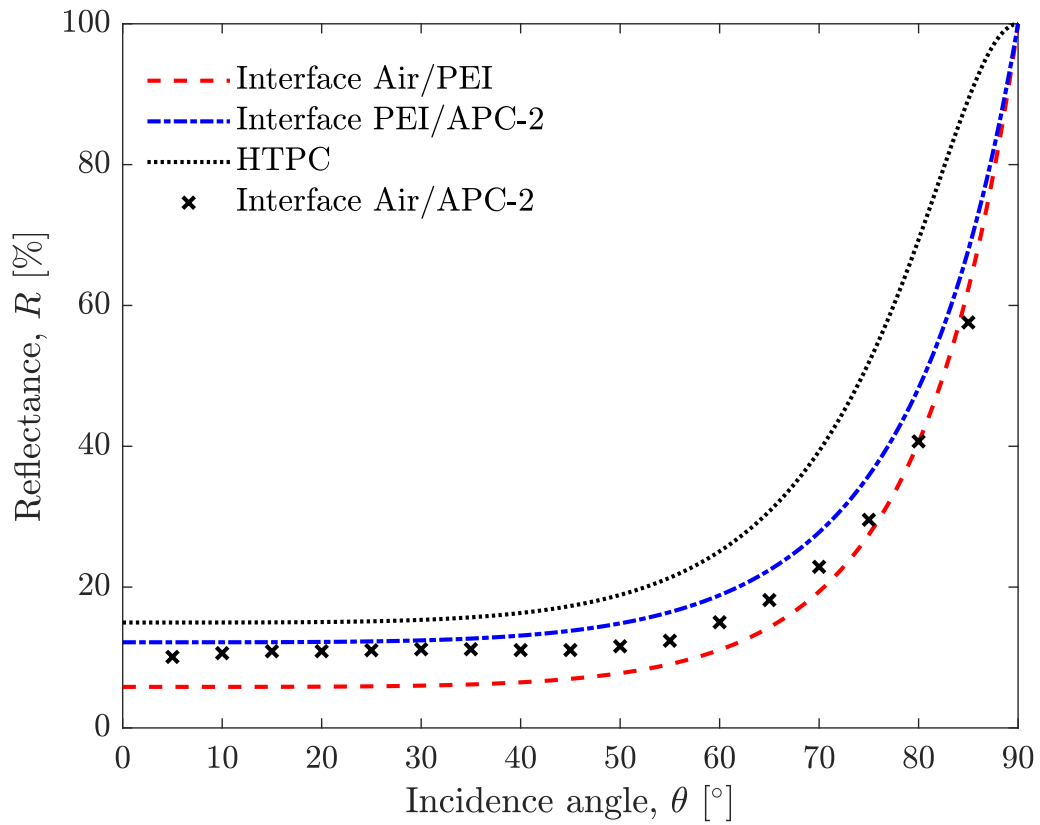


Fig. 4: Angular dependence of the reflectance for HTPC ( $\lambda = 980 \text{ nm}$ ) compared with experimental measurement for APC-2 [14]

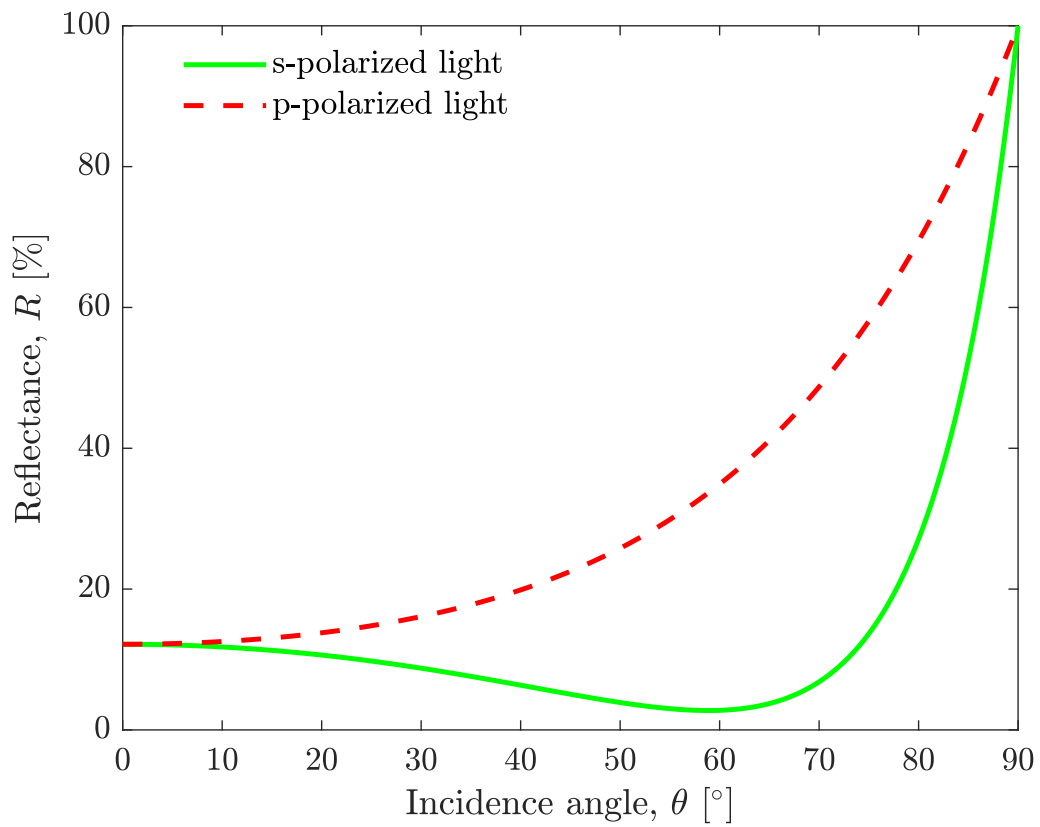


Fig. 5: Relative intensity reflectance of APC-2 with s and p-polarisation for  $\lambda = 980 \text{ nm}$

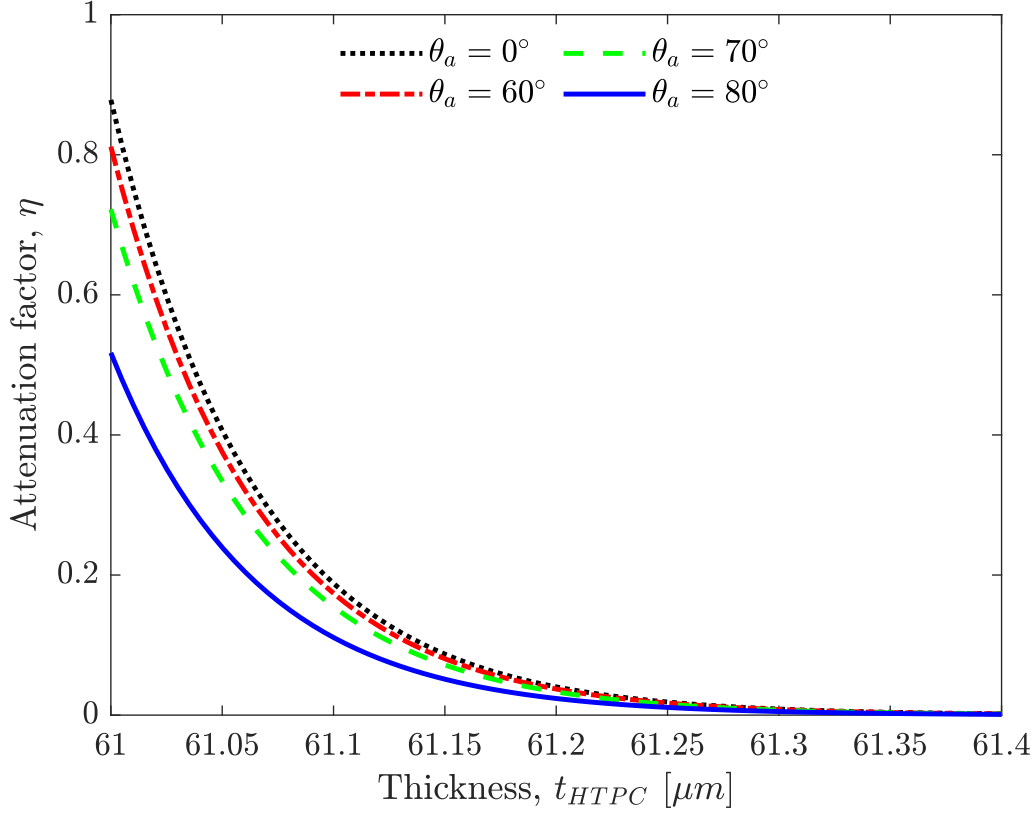


Fig. 6: Penetration depth of the irradiation in the HTPC for  $\lambda = 980 \text{ nm}$

The measurement of the emissivity is carried out for a temperature of  $T = 250^\circ C$  and for a broad spectral band  $[8 - 12] \mu m$ . The value of the emissivity of the hybrid material is estimated by minimising the error between the thermocouple temperature and the thermal infrared camera. The best correlation is obtained with  $\varepsilon = 0.87 \pm 0.01$ . However, the measured emissivity using a spectrometer ( $[8 - 12] \mu m$ ) with integrating sphere is found to be 0.02 upper than the value obtained by IR camera. This difference is explained by the contact between the thermocouple and the heating plate, which causes to overestimate the temperature. Therefore, the

190 emissivity value considered in this study is  $\varepsilon = 0.89$  obtained by spectroscopic measurement.

The data in Figs. 3 to 6 represent the main keys to investigate the laser-material interaction such as absorption, reflection and penetration depth of the irradiation into the material in a specific wavelength. The  
195 consideration of the incidence angle in this data allows to study the interaction based on parameters of the AFP robot head.

### 2.3. Thermal properties

To determine the normal absorptance  $A_n$  of the HTPC material and coefficients that described the transfer change between table and  
200 surroundings air, a 3D transient thermal model is developed and compared with experimental results. The experimental test consists of several static laser shooting during 0.2 s on sample plaque made of HTPC material with a laser power of  $P_L = 400 W$ . The optical device (8F-56-8) used in the present study is that used on the AFP machine. This optics provides a  
205 rectangular-shaped spot ( $L_x \times L_y$ ) measuring  $56 \times 8 mm^2$ . The heat source for the process is a fibre-coupled diode laser system (two diode stacks at  $\lambda \approx 980 nm$  and two at  $\lambda \approx 1030 nm$ ). The energy flow  $\Phi(x, y)$  arriving at a given point on the surface is expressed as follows

$$\Phi(x, y) = \frac{A_n \eta_{laser} P_{eff}}{L_x L_y} X(x) Y(y) \quad (5)$$

where  $\eta_{laser}$  is the loss in optical fibre,  $P_{eff}$  is the effective laser power,  $X(x)$   
210 and  $Y(y)$  are the normalized irradiation length and width profiles of the super-Gaussian beam at the focal distance, respectively. In the case of the

(8F-56-8) optics, both  $X(x)$  and  $Y(y)$  are obtained from super-Gaussian functions fitted to map the laser spot obtained from a static laser shot on a thermal sensitive paper (ZAP-IT paper). Fig. 7 shows the normalized  
 215 intensity of the laser beam at a focal distance of  $w_f = 250 \text{ mm}$ .

The temperature at the HTPC interface is measured using an infrared camera with emissivity  $\varepsilon = 0.89$ . With regard to the numerical simulation, the problem involves to perform a heating and cooling stage. Solving this problem requires the accurate knowledge of the boundary conditions. In the  
 220 first, the heat exchange between material and surrounding air is prescribed by the Newton's law,  $\overrightarrow{\varphi_{conv}} = h_c(T - T_{amb})\overrightarrow{n}$ , in which the ambient temperature is  $T_{amb} = 18^\circ\text{C}$  and  $h_c$  is the convective heat transfer coefficient. The thermal exchange between the substrate and the tooling is described by the heat transfer coefficient  $h_t$ , while the heat lost by irradiation is defined by the  
 225 following relationship

$$\overrightarrow{\varphi_{rad}} = h_{rad}(T - T_{amb})\overrightarrow{n} \quad (6)$$

where  $h_{rad}$  is the radiation exchange coefficient given by  $h_{rad} = \sigma\varepsilon(T^2 + T_{amb}^2)(T + T_{amb})$ .  $\sigma = 5.67 \cdot 10^{-8} \text{ W/m}^2 \cdot \text{K}^4$  is the Stefan-Boltzmann constant. To obtain accurate thermal distributions in the laminate, the material model must include temperature-dependent  
 230 physical properties, such as a temperature-dependent specific heat ( $C_p$ ), a temperature-dependent density ( $\rho$ ) and a temperature-dependent thermal conductivity ( $K$ ). For the APC-2 material, these properties are collected from [13] and summarised in Table 1. Then, the temperature dependence of these physical properties are obtained from a linear regression analysis.

235 Regarding the PEI material, a capillary rheometer Rheograph 20 is used  
to perform thermal conductivity and PVT measurements. Fig. 8 shows  
the curve fitting of the experimental data for both isotropic thermal  
conductivity and density as a function of temperature under atmospheric  
pressure. Fig. 9 depicts the temperature-dependent specific heat data  
240 obtained by differential scanning calorimetry (DSC).

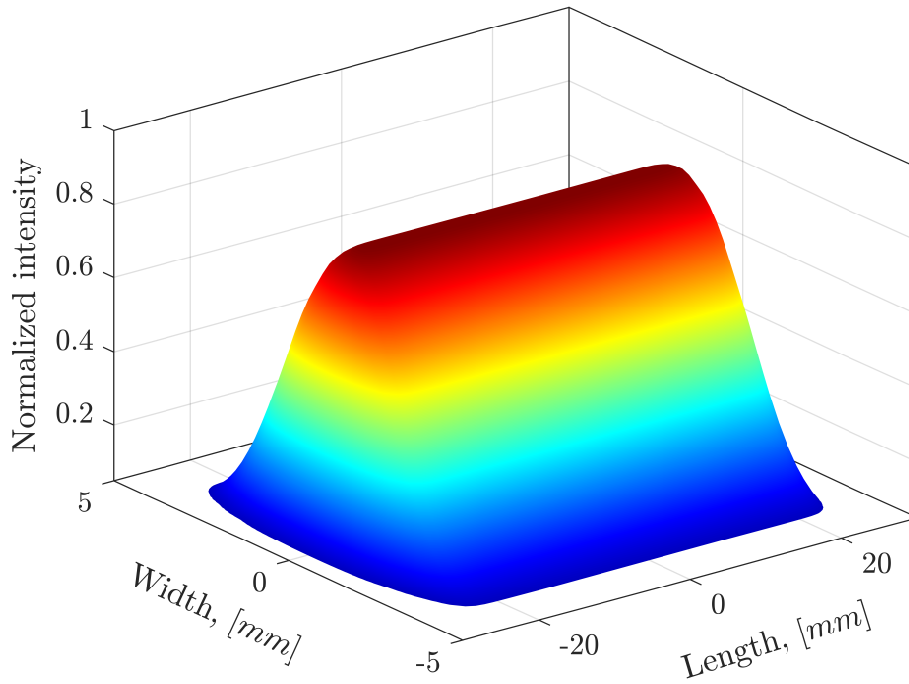


Fig. 7: Normalized irradiation of super-Gaussian beam at the focal distance  $w_f$

The normal absorptance  $A_n$  and the heat transfer coefficients  $h_c$  and  $h_t$  are determined from numerical simulations by comparing the thermal model with the experimental data. Fig. 10 shows the experimental temperature profile

and its result by adjusting the numerical model. A very good correlation is  
 245 found for  $A_n = 0.7$ ,  $h_c = 7 \text{ W/m}^2/\text{K}$  and  $h_t = 116 \text{ W/m}^2/\text{K}$ .

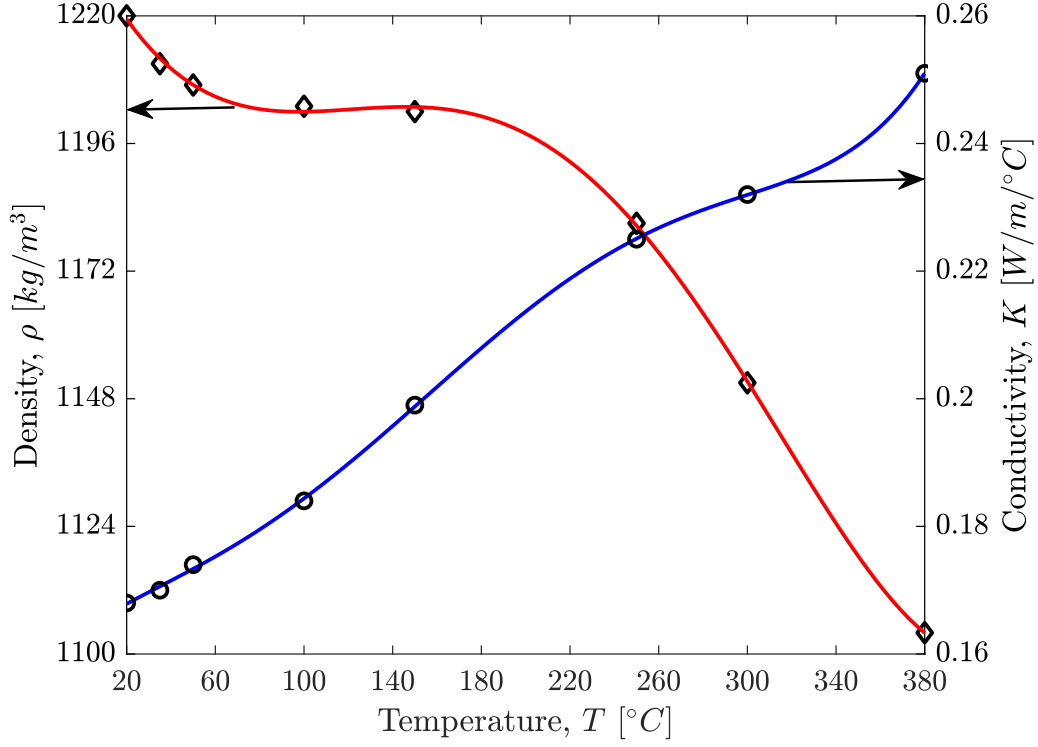


Fig. 8: Fits of measurement data of density (circle marker) and thermal conductivity (diamond marker) of PEI film

Temperature $T$ [ $^{\circ}\text{C}$ ]	Density $\rho$ [ $\text{kg}/\text{m}^3$ ]	Specific heat capacity $C_p$ [ $\text{J}/\text{kg} \cdot ^{\circ}\text{C}$ ]	Thermal conductivity	
			$K_{xx}$ [ $\text{W}/\text{m}/^{\circ}\text{C}$ ]	$K_{yy}$ [ $\text{W}/\text{m}/^{\circ}\text{C}$ ]
23	1540	1100	4.92	0.61
400	1524	1800	7.68	0.66

Table 1: Physical properties of APC-2 at  $23^{\circ}\text{C}$  and  $400^{\circ}\text{C}$

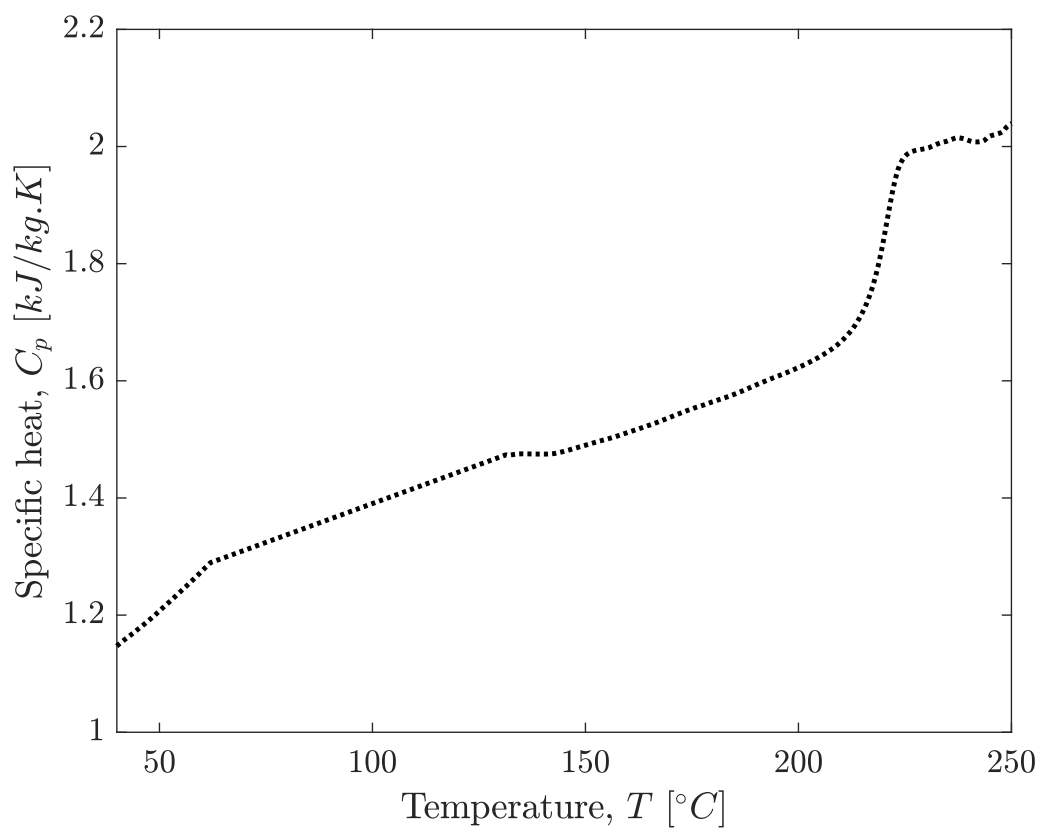


Fig. 9: Measurements of specific heat of PEI

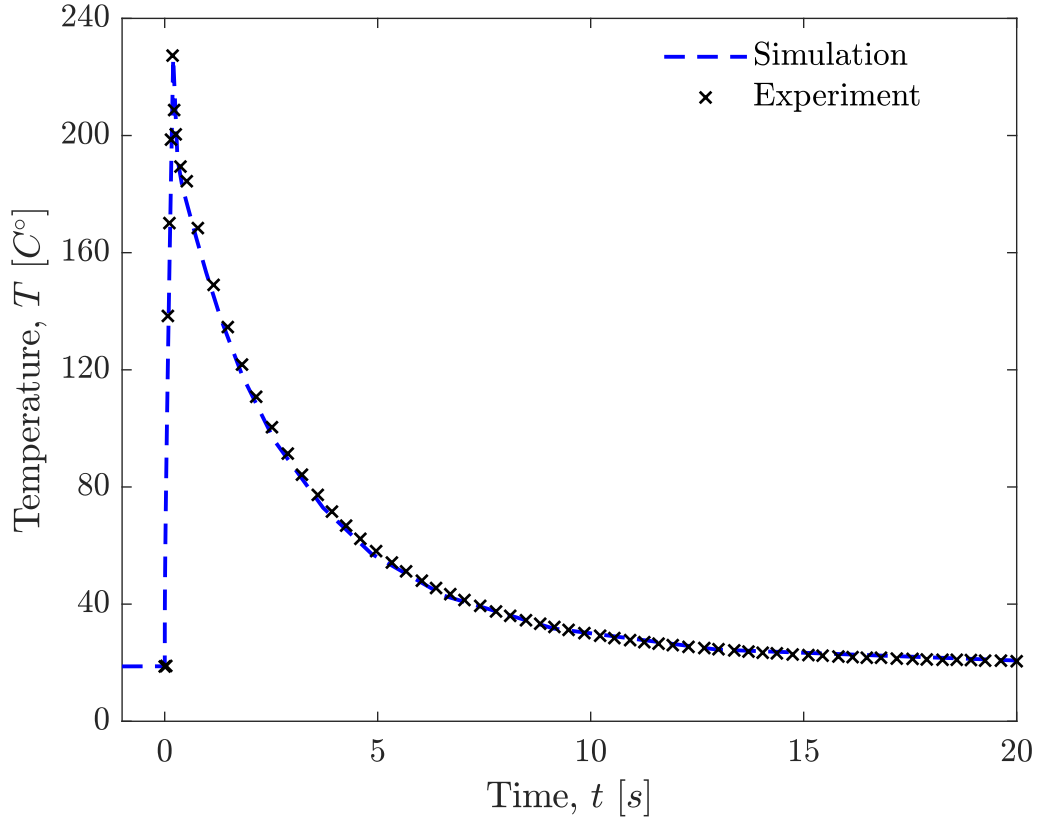


Fig. 10: Correlation between experimental and numerical temperature profiles

### 3. Thermo-optical model

#### 3.1. Ray-tracing method

To model the laser-material interaction during the process, a ray-tracing method has been implemented, which allows computing the laser distribution on the substrate and incoming tape. To simplify the analysis, the specular reflection approach is used based on previously validated models for flat and curved geometries [32, 33, 17]. The AFP head parameters are considered, such as laser power  $P_L$ , incident angle  $\beta$  and tilt angle  $\theta$  of the robot head.

Furthermore, the roller deformation under the compaction force  $F$  is also taken into account to evaluate the reflection phenomena as function of roller profile. Based on contact mechanics [34], the roller profile of a commercial silicone roller can be written as follow [17]

$$g(x, F) = \begin{cases} \frac{(\delta - R_r)}{(R_r - w(F))^2} \sqrt{(R_r - w(F))^2 - \left(x - \frac{|x|}{x} w(F)\right)^2} & \forall z < 0 \quad (a) \\ \delta - R_r & \forall z < 0, \forall |x| < w^F \quad (b) \\ \sqrt{R_r^2 - x^2} & \forall z > 0 \quad (c) \end{cases} \quad (7)$$

where  $R_r$  is the radius of the roller,  $w(F) = (4R_r F \cos(\theta) / \pi E_{eq} L)^{1/2}$  is the half-contact between the roller and a rigid flat substrate, in which  $E_{eq}$  is the equivalent Young modulus of the roller.  $\delta$  is the the radial deformation given by [35, 36].

In the first step of the ray-tracing method, the laser beam from the optical source onto both tape and substrate is divided into  $n$  rays according to the focal distance  $w_f$ . Each ray is defined by s and p-polarisation vectors. To consider the super-Gaussian profile Fig. 7, a weight is attribute to each ray from the laser source. The initial ray is assigned a fixed amount of energy depending on the intensity distribution pattern of the beam spot. Then, after setting AFP parameters, both substrate and incoming tape are meshing. The pseudo-code of this ray-tracing algorithm is illustrated in Table 2. In the second step, a mathematical test is carried out to identify the limit incident angle  $\beta_l$  between the substrate and the tape. Therefore, for each light, a logical test is performed to check whether it reaches the substrate or the tape. If the light achieved the substrate or the tape, a portion of its energy is absorbed by carbon fibres depending on its incidence angle. The part

265 of the energy reflected by the PEI or APC-2 interfaces could be absorbed  
by the tape or substrate. The absorbed energy is then calculated using the  
conservation of energy  $A+R+T = 1$ , where  $A$  and  $T$  are the absorptance and  
transmittance, respectively. The reflectance  $R$  of each ray is calculated using  
Fresnel coefficients for the s- and p-polarised lights [37]. The path of each  
270 reflected light from the substrate onto the tape and vice versa is based on the  
Snell's law. These operations are repeated for all emitted and reflected lights  
until the amplitude of their energy becomes negligible. Energy from reflected  
lights that have not reached the substrate or the tape is considered lost. The  
real reflection phenomenon with standard configuration, i.e., the incident  
275 angle  $\beta = 14.75^\circ$ , the aperture angle for the laser beam source  $\gamma = 2.03^\circ$  and  
the focal distance of the laser optics  $w_f = 250 \text{ mm}$ , is illustrated in Fig. 11.  
In the third step, the total laser heat-flux distribution in the substrate and  
the tape is calculated by computing the amount of energy accumulated on  
each element.

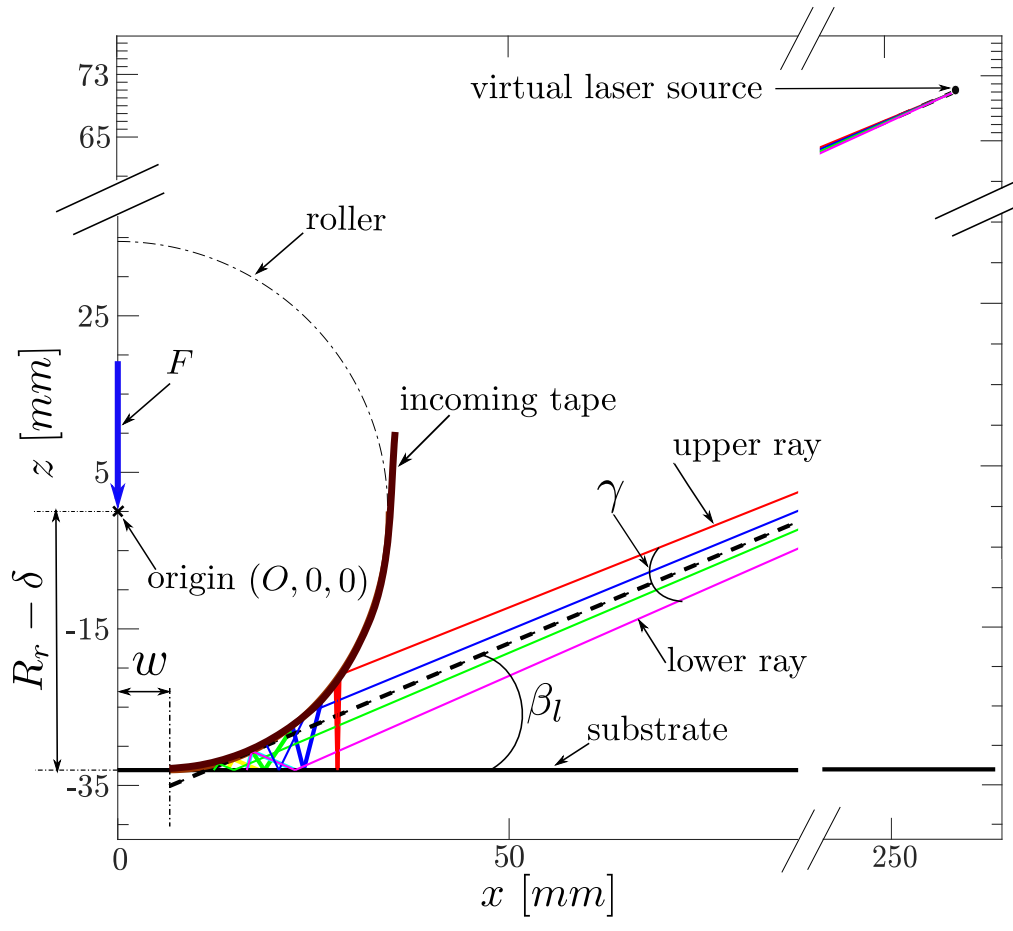


Fig. 11: Schematic representation of the incoming tape and the substrate reached by direct rays and its reflections according to the limit incident angle  $\beta$  and compaction force  $F$

---

**Algorithm 1:** Ray-tracing algorithm

---

mesh the substrate and the incoming tape

**Input** : A list of parameters:  $[\beta, w_f, L_{spot}, P_L, F]$

**Output:** Heat flux distribution:  $[\varphi_{tape}, \varphi_{substrate}]$

$newList = []$

Divide the laser beam into  $n_r$  light and calculate its corresponding incidence angle  $\theta_r$ ;

Search the limit angle tape/substrate  $\beta_l$ ;

Set the number of considered reflection  $N_{ref}$ ;

**for**  $i \leftarrow 1$  **to**  $N_{ref}$  **do**

**for**  $j \leftarrow 1$  **to**  $n_r$  **do**

**if**  $i=1$  **then**

            Establish the equation of direct light  $L(i, 1)$ ;

**if**  $\theta_r \leq \beta_l$  **then**

            Compute the reflected and the absorbed  $E_t(i, 1)$  energy by tape;

**else**

            Compute the reflected and the absorbed energy  $E_s(i, 1)$  by substrate;

**end if**

**else**

        Establish the equation to reflect light  $L_r(i, j)$ ;

        Check the interaction between the substrate or the tape;

        Compute the reflected and the absorbed energy  $E_s(i, j)$  or

$E_t(i, j)$ ;

**end if**

        Update the  $newList \leftarrow \{[E_t(i, j), E_s(i, j)]\}$ ;

**end for**

**end for**

Compute the accumulate energy in each element of the substrate and the tape; **return**  $\varphi_{tape}, \varphi_{substrate}$

---

Table 2: Ray-tracing algorithm

The thermal distribution induced in the substrate during AFP process is represented by a 2D numerical model, given the small thickness of a ply when compared to its width. In addition, the choice of the 2D problem is suitable for establishing the process window. This model is coupled with the non-uniform incident heat flux distributions estimated by ray-tracing method, including the process parameters. In a moving domain, the governing heat transfer equations for the anisotropic hybrid material can be written in a Lagrangian approach as

$$\begin{cases} \rho_{PEI} C_{p,PEI} \dot{T}(x_0, z_0, t) - K_{PEI} \Delta T(x_0, z_0, t) = 0 & z_0 \in t_{PEI} \\ \rho_{APC-2} C_{p,APC-2} \dot{T}(x_0, z_0, t) - \text{div}(\overline{\overline{K}}_{APC-2} \cdot \overrightarrow{\text{grad}} T(x_0, z_0, t)) = 0 & z_0 \in t_{APC-2} \end{cases} \quad (8)$$

where  $C_p$ ,  $\overline{\overline{K}}$  and  $\rho$  are the specific heat capacity, the thermal conductivity tensor (that becomes isotropic for the PEI) and the material density, respectively, which are considered to be temperature-dependent as discussed previously. The various heat losses that occur during the AFP process are described by the following equations

$$\begin{cases} \varphi_{conv} = h_c(T - T_{amb}) & \text{on } D_c \\ \overrightarrow{\varphi_{rad}} = h_{rad}(T - T_{amb}) \overrightarrow{n} & \text{on } D_c \\ \varphi_t = h_t(T - T_t) & \text{on } D_{table} \\ \varphi_r = h_r(T - T_r) & \text{on } D_{roller} \end{cases} \quad (9)$$

These thermal losses are depicted in Fig. 12.  $D_c$  is the convection and surface-ambient radiation domain.  $h_c$  and  $h_t$  are the convection and the conduction coefficients, respectively. Since one dimension is neglected, the

value of  $h_c$  and  $h_t$  found in the subsection 2.3 are changed from  $7 W/m^2/K$  to  $15 W/m^2/K$  and  $116 W/m^2/K$  to  $410 W/m^2/K$ , respectively. These new values are determined numerically by fitting the 2D numerical model to the experiment data presented in Fig. 10, while the radiation effect adopted for the 3D model is used without any modification. In addition, at  $t = 0$ , the initial temperature distribution is assumed to be equal to the ambient temperature ( $T_{amb} = 23 \text{ }^\circ C$ ). The laser flux distribution is implemented as boundary conditions in the form of the heat flux distribution  $\varphi^{i,j} = -P^{i,j}/S^{i,j}$  for each element  $i$  reached of the substrate or  $j$  of the incoming tape, which  $P$  represents the total accumulated energy on the surface  $S$  of the element.

For a quasi-static analysis, the heat transfer is modelled by an Eulerian approach in which the reference  $(O, x, z)$  is related to the head velocity. Then, the steady-state heat transfer problem may be written as

$$\begin{cases} \rho_{PEI} C_{p,PEI} V \frac{\partial T(x,z)}{\partial x} - K_{PEI} \Delta T(x, z) = 0 & z \in t_{PEI} \\ \rho_{APC-2} C_{p,APC-2} V \frac{\partial T(x,z)}{\partial x} - \text{div}(\overline{\overline{K}}_{APC-2} \cdot \overrightarrow{\text{grad}} T(x, z)) = 0 & z \in t_{APC-2} \end{cases} \quad (10)$$

where  $V = dx/dt$  is the layup velocity of the process. The advantage of the quasi-static analysis compared to the transient model is the computation time, which can be very useful to control the temperature.

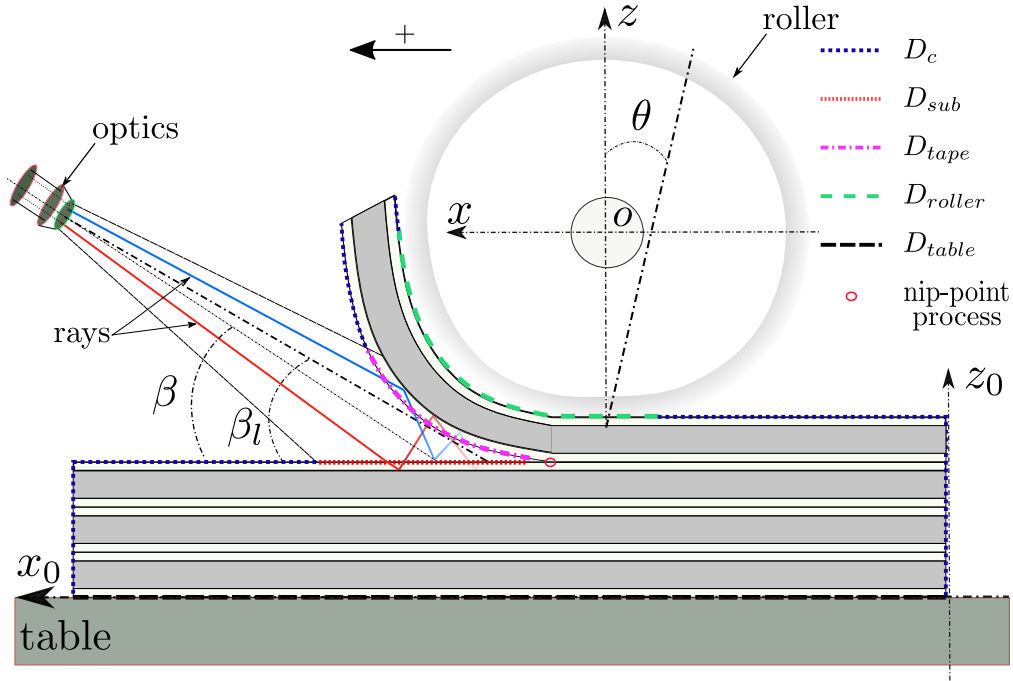


Fig. 12: Boundary conditions

## 4. Comparison between experiment and numerical predictions

### 4.1. Experimental setup

315 A fibre placement machine developed by Coriolis Composites is used to conduct the experimental tests (see Fig. 13). The placement head is mounted on a six-axis robot, on which is fixed a conformable silicone consolidation roller coated with non-adhesive perfluoroalkoxy (PFA). The optical device (8F-56-8) is mounted in the robot head to heat both the substrate and the  
 320 incoming tape according to the incident angle  $\beta$ . This optic generates a constant rectangular spot with an aperture angle of  $2.03^\circ$ . At the focal distance  $w_f = 250 \text{ mm}$ , the size of laser spot is about  $56 \times 8 \text{ mm}^2$  with a

super-Gaussian intensity distribution as shown in Fig. 7. A FLIR IR-camera is installed next to the optics on the head to monitor the temperature during  
325 the layup near the nip-point process. The purpose of the application is to use a laser a diode laser power to heat the HTPC up to a process temperature (between the  $T_g$  of PEI and  $T_m$  of PEEK). The size of the draping geometry is  $500 \times 500 \text{ mm}^2$ . At the start of the test, the first layer of HTPC ( $600 \times 600 \text{ mm}^2$ ) produced by Novotech Aerospace Advanced  
330 Technology (see Fig. 14) is fixed on the table. Then, a couple of K-type thermocouples ( $80 \mu\text{m}$  in diameter) with a rapid response is inserted during the layup according to the arrangement presented in Fig. 15. To avoid excess thickness accumulation, the offset  $x_0$  is taken into account before adding each thermocouple. The temperature was recorded during the process (at a  
335 frequency of  $300 \text{ Hz}$ ) using a universal QuantumX data acquisition system. The standard process parameters used are reported in Table 3. The laser beam strikes equally the substrate and the incoming tape for this default configuration.

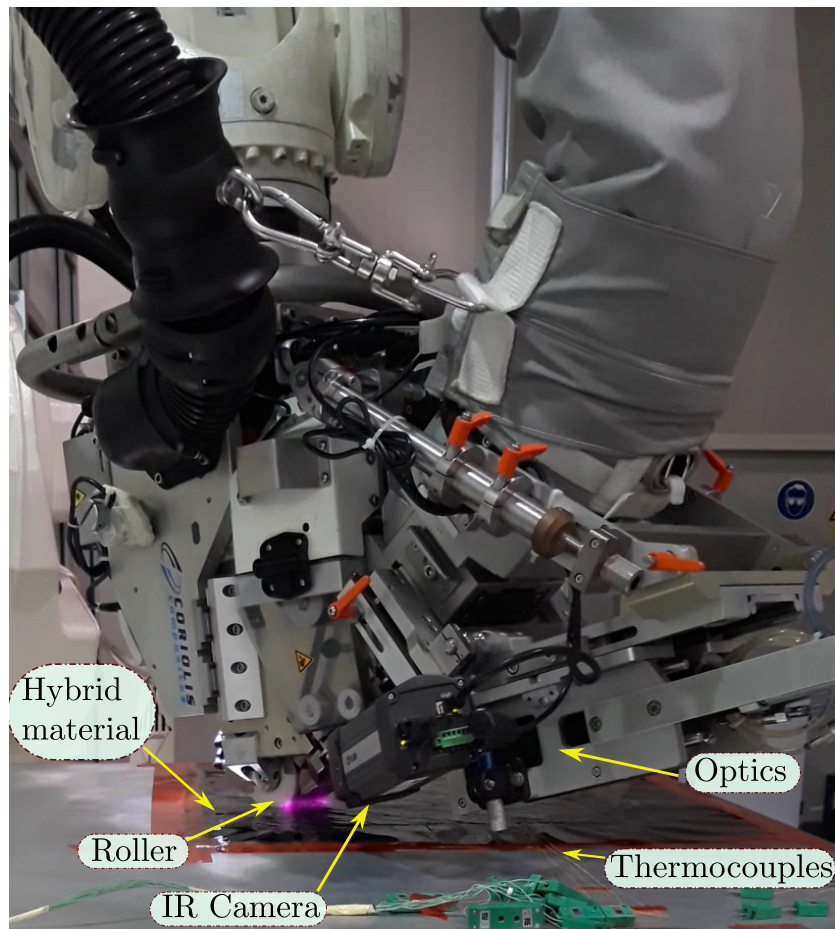


Fig. 13: In-situ AFP process showing the layup of the hybrid material with thermocouples



Fig. 14: The NOVOTECH press which produced the hybrid material

Parameter	Symbol	Value
Laser power	$P_L$	3 kW
Laser power efficiency	$\eta_{laser}$	80 %
Process speed	$V$	0.2 m/s
Tilt of head	$\theta$	7°
Incident laser angle	$\beta$	14.75°
Compaction force	$F$	250 N

Table 3: Experimental process parameters

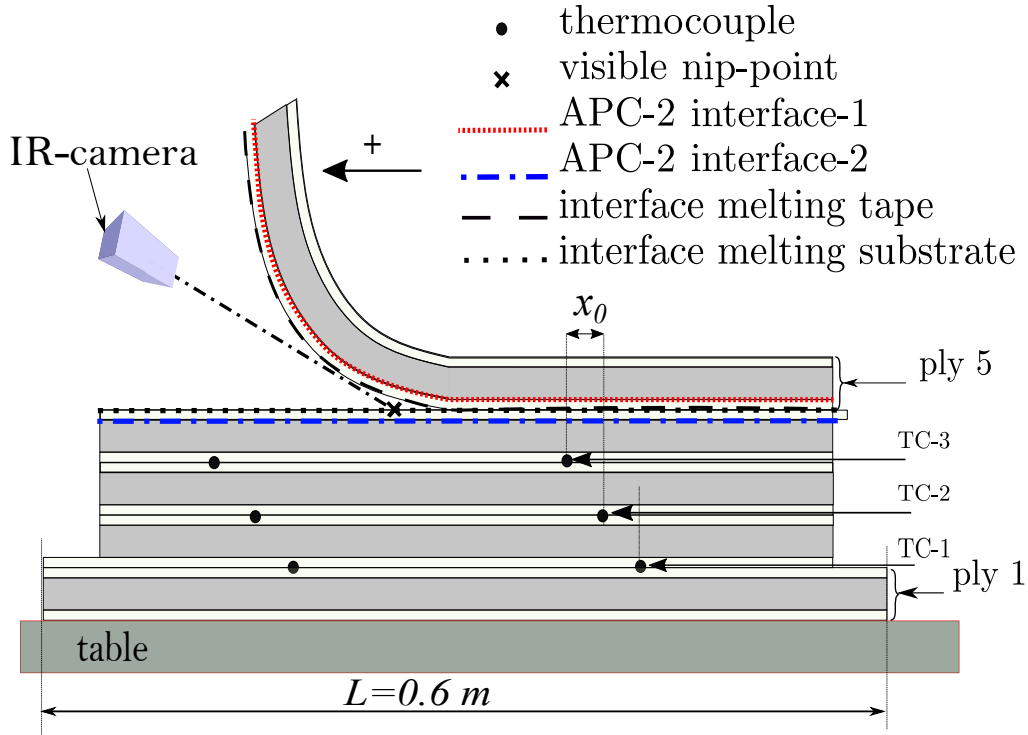


Fig. 15: Experimental design

#### 4.2. Numerical model implementation

340 Fig.16 is a flow diagram illustrating the overall steps for obtaining the thermal results. After identifying the process and robot head parameters, the roller deformation should be calculated based on the roller properties, the compaction force and the tilt of the head. Then, the nip-point process and tape profile can be identified from the roller profile. The tape and the  
 345 substrate are then discretized, followed by the execution of the ray-tracing algorithm to compute the total energy absorbed on each element. In this step, the laser beam is split into  $n_r = 50000$  rays to achieve an accurate heat flux distribution on the tape and the substrate. Thereafter, to describe

the orthotropic thermal properties of the HTPC material, the finite element software Abaqus is employed. The moving heat flux distributions at each element of the incoming tape ( $\varphi_{tape}$ ) and the substrate ( $\varphi_{sub}$ ) are implemented using the DFLUX user subroutine, while the convection and radiation heat losses are developed in the FILM user subroutine. The following assumptions are also made

- The friction between the roller and the tape is negligible.
- The contact between the PEI and the APC-2 is assumed perfect.
- The incoming tape is considered to be aligned with the laying direction.

The third assumption is used to simplify the thermal problem without affecting the real model. In this case, the incoming tape is placed on the substrate. To avoid the conduction of heat exchange between the incoming tapes and the substrate, an infinite thermal resistance (IRTC in Fig.18) is introduced at this contact from the nip-point process. The inter-ply thermal contact resistance of the substrate is calculated as a function of degree of intimate contact  $D_{ic}$  as introduced by Levy et al. [38]. The surface roughness parameters of the PEI film are collected from [39]. Therefore, the evolution of thermal contact resistance is coupled with the heat transfer problem via the user subroutine GAPCON.

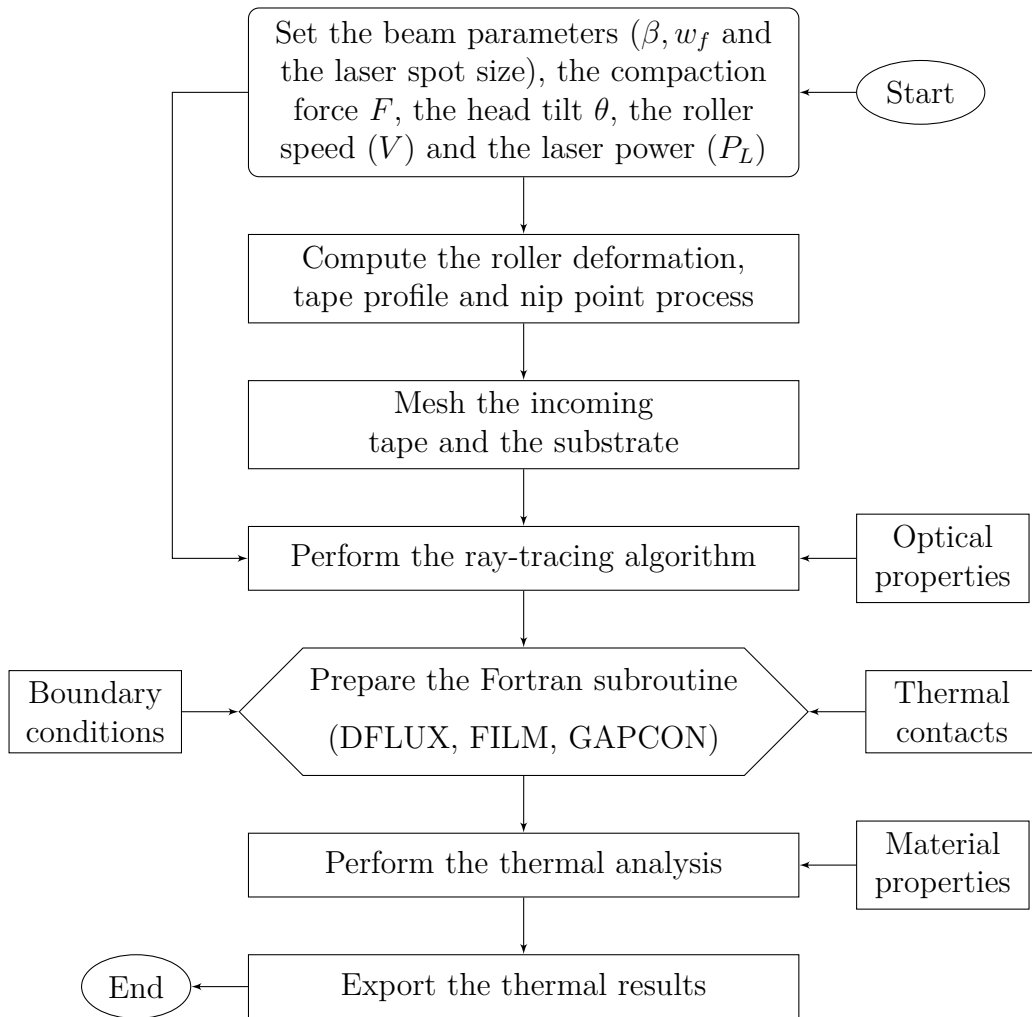


Fig. 16: Flow diagram of the thermo-optical model

#### 4.3. Results and discussion

The laser distribution plot for the experimental process parameters is presented in Fig. 17, in which the total incident heat flux on the substrate and the incoming tape from nip-point process computed from the ray-tracing method are depicted. The obtained profile shows that the illuminated area

on the tape is larger than the substrate area, despite the standard process parameters in Table 3 are set to obtain an even distribution on the substrate  
375 and the incoming tape. This is because the reflection phenomenon occurs near the nip-point process. It is found that there are three reflections from the substrate or the incoming tape until the intensity of the light is attenuated by the HTPC. Light is absent at a distance of  $x = 3 \text{ mm}$  due to shadow region starting from the nip-point process to the visible nip-point. The data for the  
380 total heat flux are then injected on the thermal model. Fig. 18 shows the simulation results for the standard configuration. To facilitate visualization temperature field following the thickness of the plate length of  $0.5 \text{ m}$ , a ratio 130 is applied in the  $z_0$  direction. From this mapping, the temperatures at the interface melting and between plies are extracted and compared to the  
385 experimental results.

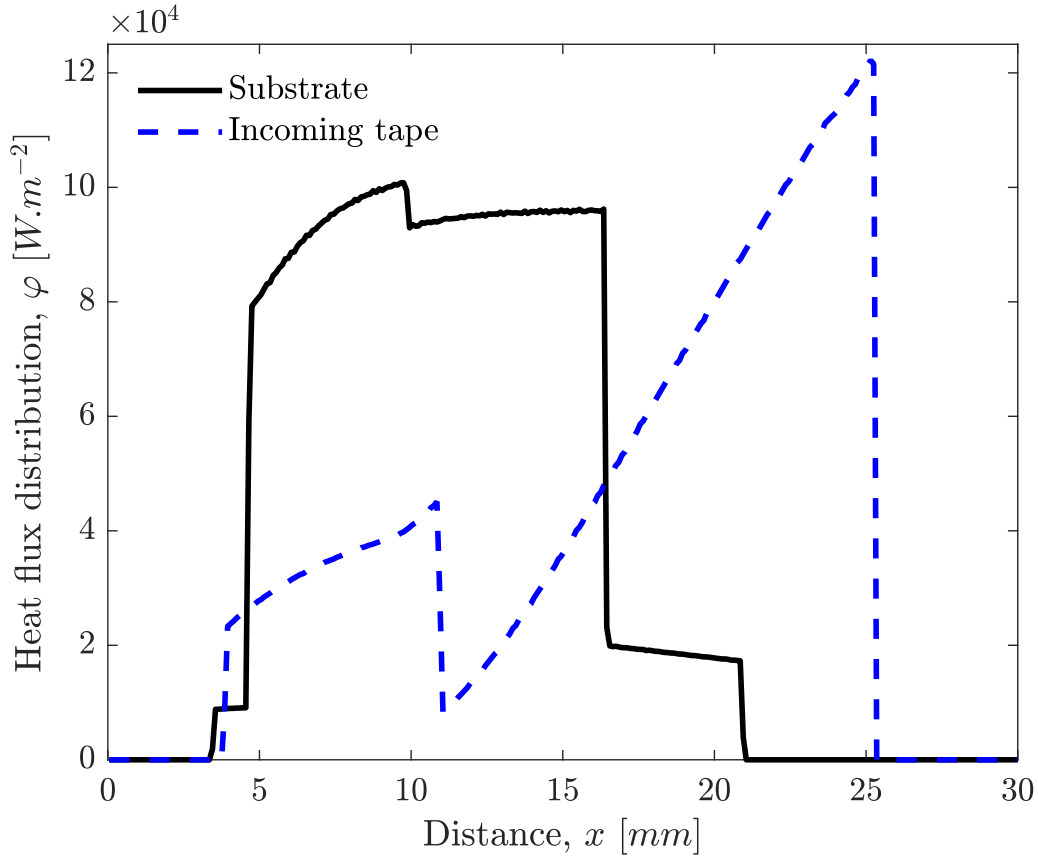


Fig. 17: Total incident heat flux on the substrate and the incoming tape for the experimental parameters listed in Table 3. The distance from nip-point process is shown in Fig. 12

Fig. 19 illustrated the evolution of the inter-layer average temperature during draping the fifth layer. The obtained results show the good agreement between the FEM predictions and the experimental data in terms of the timing and average maximum temperature. In addition, the difference between measurements and predictions for the thermal history is less than 6 °C. It is important to note that the temperature measured at the heated

390

interface between the substrate and the tape by thermocouples is affected by the laser beam which displays error value. This is due to the absorption of irradiation by thermocouples when placed on the substrate. However, 395 the measured temperature at the visible nip-point process is recorded by a IR-camera (mounted on the placement head in parallel with the optical laser) and compared to numerical results. Fig. 20 depicts the numerical temperature history along the interface melting. It is found that the measured average maximum temperature is 295 °C, while the one computed 400 numerically equals 286 °C. This difference is due to the fact that the IR camera measures also the temperature emitted by the APC-2 interface, which equals 348 °C at the APC-2 substrate interface and 243 °C at the APC-2 tape interface. On the other hand, in the consolidation region, the interface melting temperature is higher than the glass-transition temperature of the 405 PEI, which starts from 283 °C for the substrate and 273 °C for the tape. Moreover, the maximum temperature is located in the substrate specifically on the APC-2 interface with a value about 348 °C. This value of temperature exceeds the melting temperature of APC-2 (343 °C), which means that the APC-2 behaviour can be affected using the standard configuration.

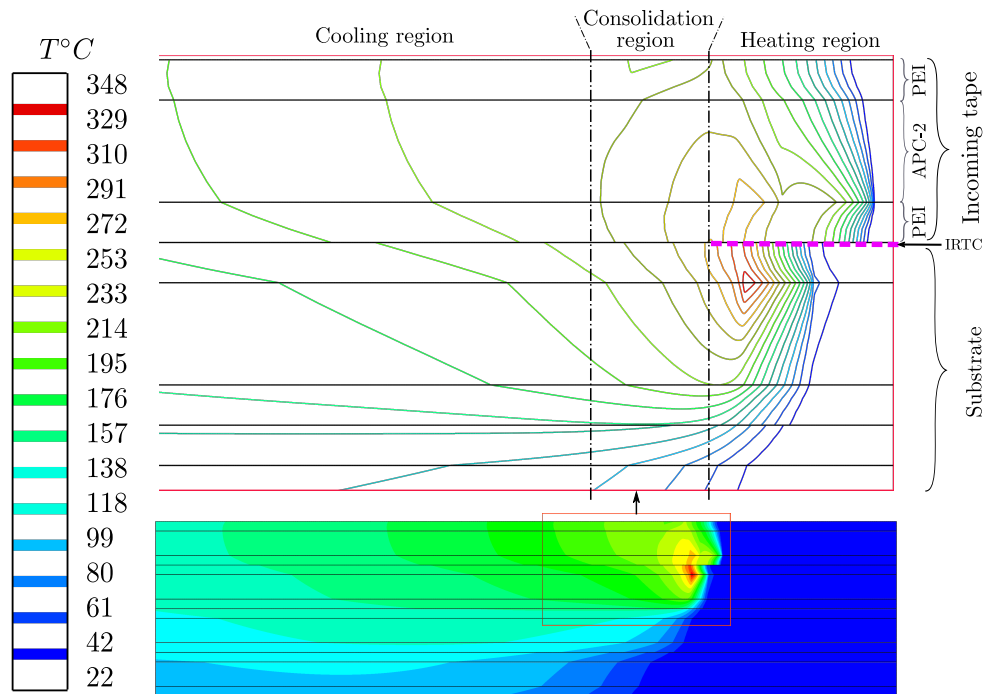


Fig. 18: Temperature distribution in the substrate and the incoming tape obtained at  $t = 1.75$  s using the standard configuration 3. A ratio 130 is applied according to the thickness of the layers

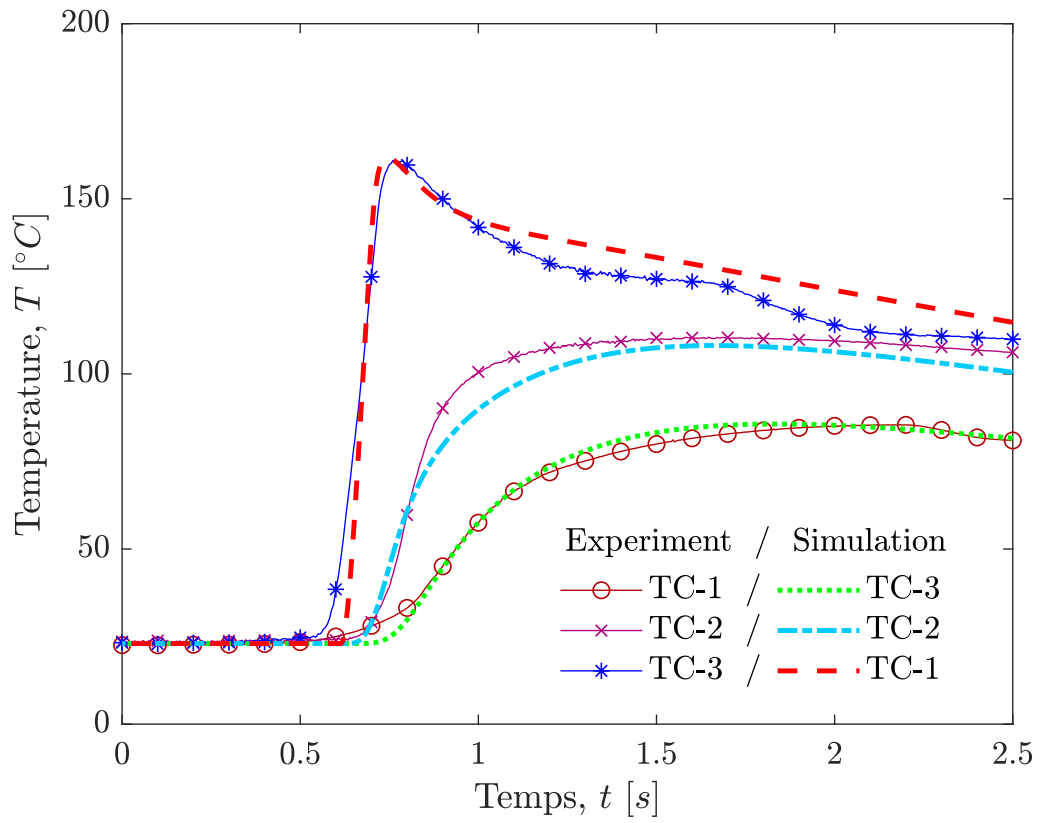


Fig. 19: Experimental and predicted thermal history between three layers of the laminate

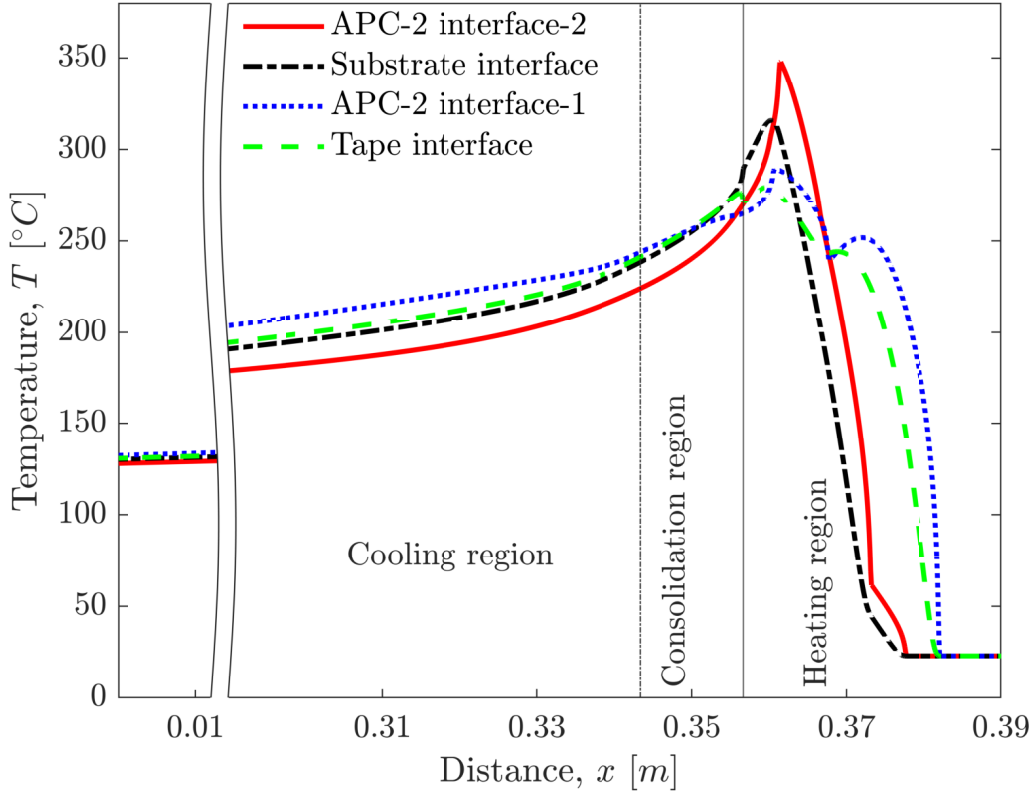


Fig. 20: Thermal history along the melting interface of PEI and APC-2 during welding the fifth layer for the experimental process parameters

410 In order to illuminate both substrate and incoming tape surfaces evenly, an optimal configuration is found by setting the incident angle at  $\beta = 15.05^\circ$  and the tilt of the robot head at  $\theta = 4^\circ$ . These values are found by using the ray-tracing method. Thereafter, the optimal incident heat flux is plotted in Fig. 21 and the corresponding temperature profile is shown in

415 Fig. 22. It can be observed that the incident heat flux on the substrate is increased and more heat is accumulated near the nip-point process. For the optimal configuration, the temperature at the nip point process is shifted

to  $297\text{ }^{\circ}\text{C}$  on the substrate. This is explained by the depth of penetration which increases with increasing the incident angle (see Fig. 6). Moreover, according to Weiler et al. [19], the depth of penetration also depends on the irradiation time, which means that the peak of the incident flux on the tape represented in Fig. 17 has a weak effect on the thermal penetration. This is confirmed by a slight increase at distance  $x_0 = 0.38\text{ m}$  (see Fig. 20) for the maximum distribution of the heat on the tape  $\varphi_{tape} = 12.22 \times 10^4\text{ W/m}^2$ . From the Fig. 22, the temperature on the APC-2 interface exceeds the melting temperature of PEEK. To minimize this temperature below the PEEK melting temperature, the laser power is reduced to  $P_L = 2750\text{ W}$ . For this update power, the average temperature near the nip point process is approximately  $270\text{ }^{\circ}\text{C}$  on the substrate, while the maximum temperature on the APC-2 interface is about  $336\text{ }^{\circ}\text{C}$ .

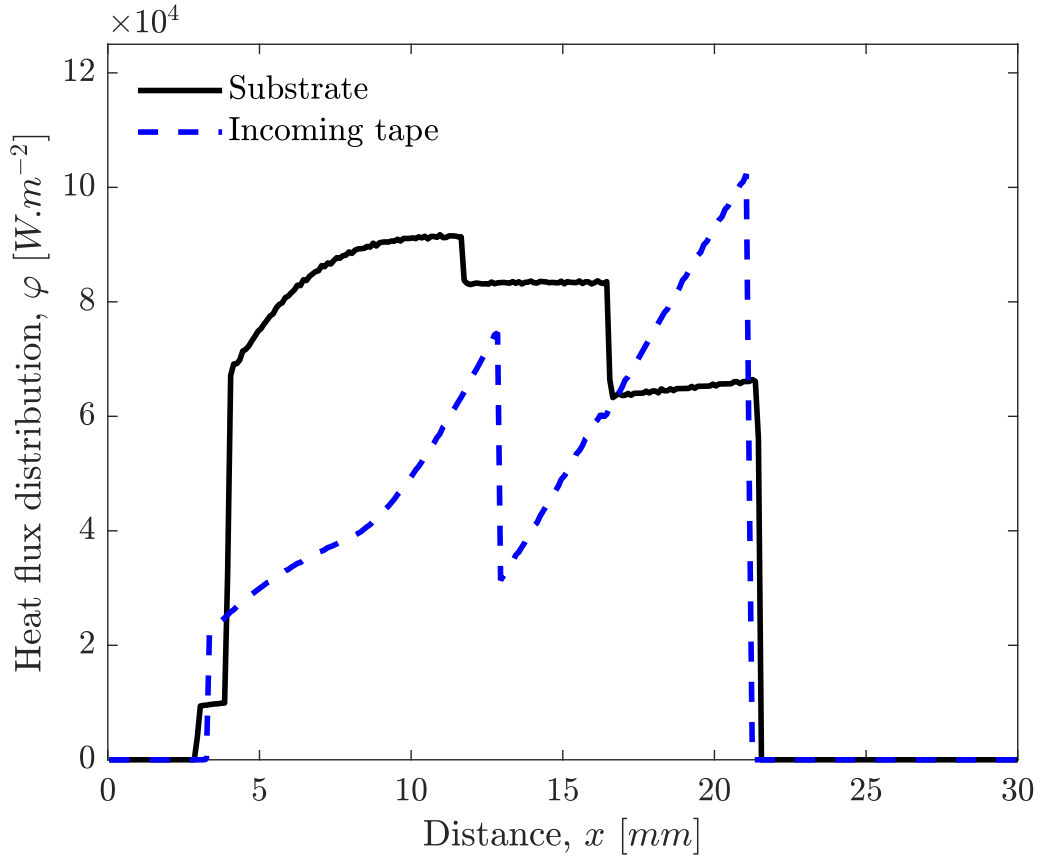


Fig. 21: Optimal incident heat flux on the substrate and the incoming tape. The compaction force and the tilt of the head are  $F = 250 \text{ N}$  and  $\theta = 4^\circ$ , respectively. The input laser power is  $P_L = 3 \text{ kW}$  with an optimal laser angle of  $\beta = 15.05^\circ$

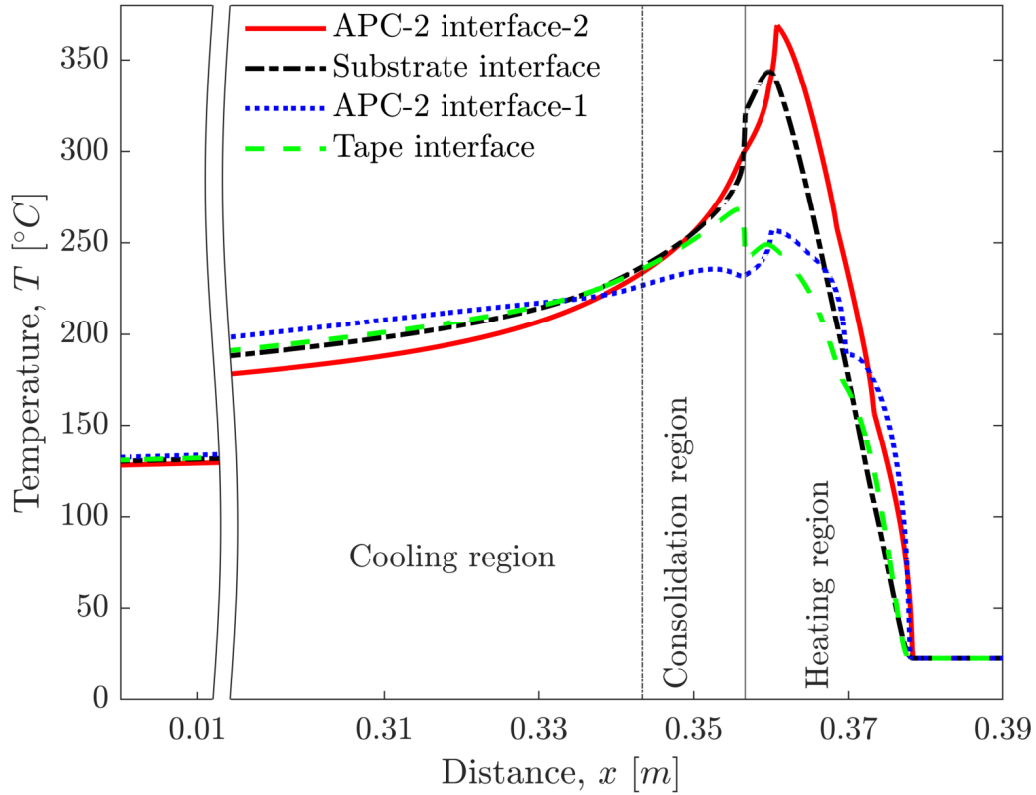


Fig. 22: Thermal history along the melting interface of PEI and APC-2 during welding the fifth layer for optimal process parameters

In Fig. 23 and with the optimal process parameters, the maximum temperature in the consolidation region (i.e., in layer 5) is plotted for various speeds and laser power. The obtained curves show a quasi-linear relationship between the laser power and the maximum temperature for each speed. In addition, the slope of each curve decreases with increasing the laser power. This is because the extremely short process time, which considerably affects the penetration depth of the irradiation into the material at higher speed, as demonstrated by Weiler et al. [19]. In order to establish a heating law

for the HTPC material, a linear regression for each curve is used to obtain  
440 the correlation between the layup speed and power laser need to maintain  
a constant temperature at the nip-point process. In the present work, this  
temperature is set at 250 °C near the nip-point process.

Two main reasons for which this material was developed are the  
improvement of the adhesion between layers thanks to an amorphous material  
445 on the surface and to control the rate of crystallinity of the APC-2. In fact,  
the aeronautical industry closely monitors the rate of crystallinity of APC-2  
processed by additive manufacturing processes. The objective is therefore to  
melt the PEI in order to achieve good adhesion between layers and not to  
melt the APC-2 so as not to modify its degree of crystallinity. A serie of  
450 calculations was performed to obtain a temperature of 250 °C at the nip-point  
process. For each of these calculations, the temperature of the APC-2 is  
noted. In Fig. 24 are presented the laser power/process speed operating  
points to reach 250 °C and for each of these points, the temperature of  
APC-2 is reported. It is noticed that beyond a speed of 0.5 *m/s*, the APC-2  
455 is melted in the process. In order to avoid the melting temperature of PEEK,  
the limit interval associated with the nip-point process temperature measured  
at APC-2 interface is estimated through a series of calculations using the  
steady state analysis and the optimal configuration. The results reported in  
Fig. 24 shown that a limit isothermal (343 °C) melting temperature of APC-2  
460 is closed to the 250 °C at nip-point process.

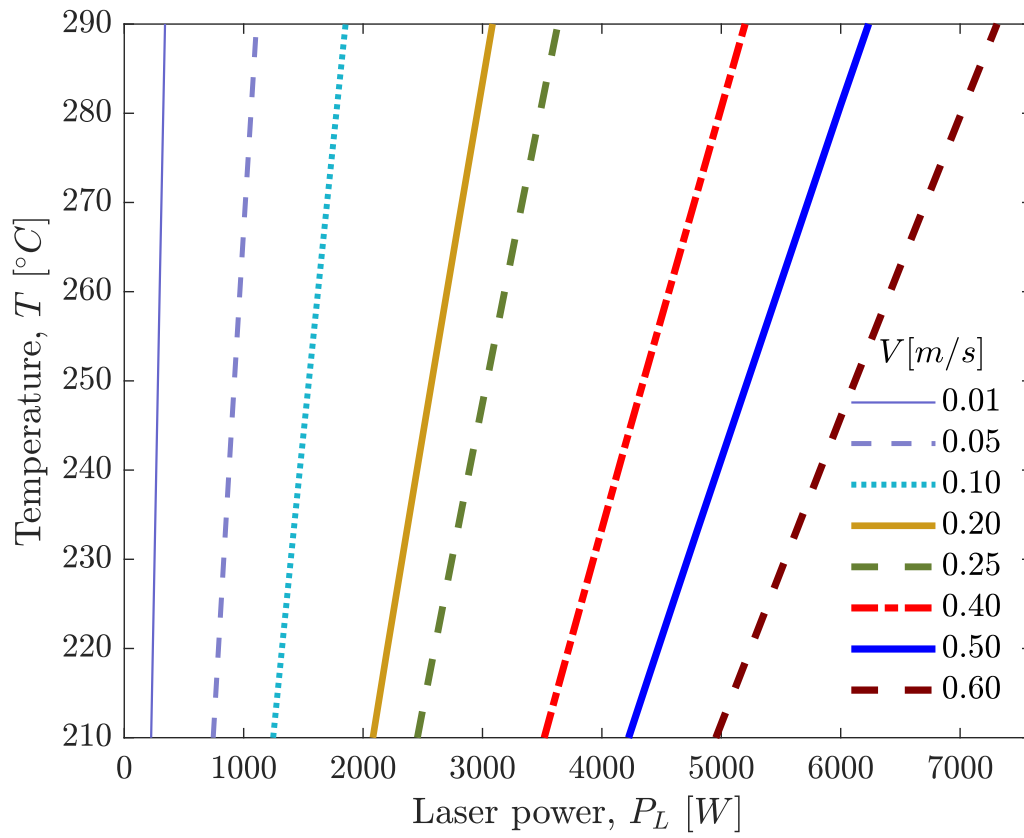


Fig. 23: Correlation between the laser power and temperature at the nip-point process for the optimal process parameters. The values is computed from the quasi-static analysis

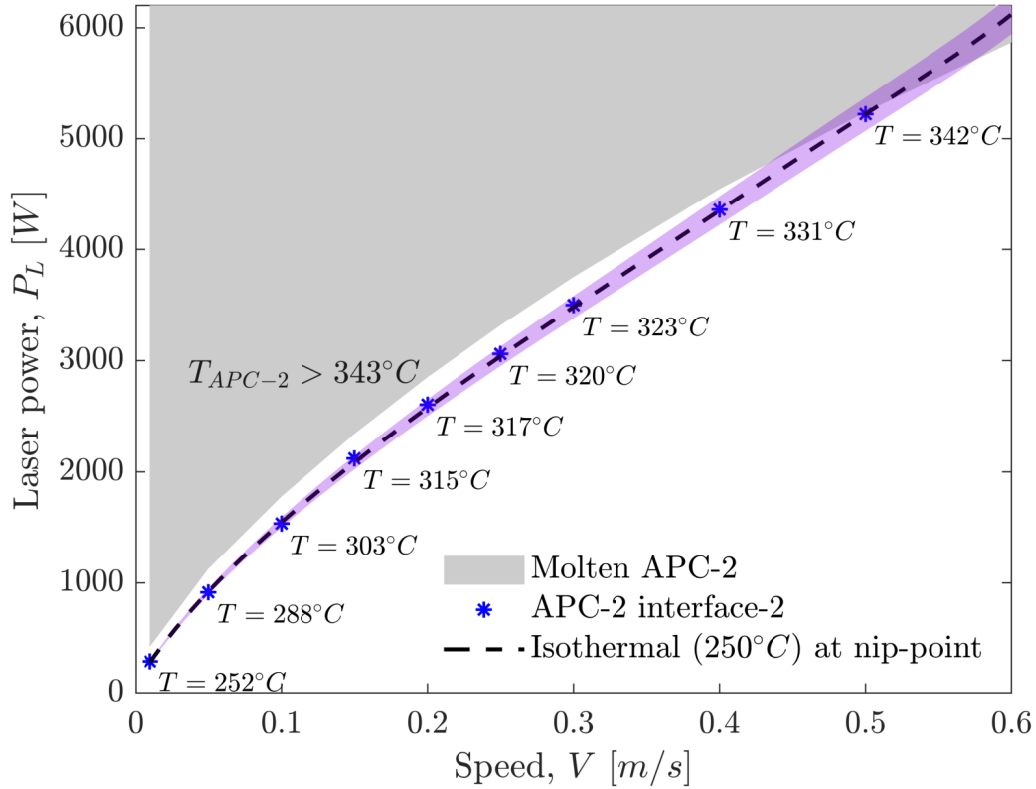


Fig. 24: Correlation between the laser power and layup speed to obtain a constant temperature of  $250^{\circ}\text{C}$  at nip-point process. The shaded area represents the 93% confidence interval.

## 5. Conclusion

For a AFP process, there are two mainly parameters that control the temperature distribution at the nip-point process, namely, the laser power and the layup speed. To investigate the effect of these parameters along with other parameters related to the robot head, the optical and thermal properties of the hybrid material have been characterised, and provide the basis for the optico-thermal model. For the HTPC material, it was found

that the absorption of laser beam is governed by the APC-2, specifically by the carbon fibres. The amount of absorbed energy is affected by the  
470 reflectance at the interface between the PEI film and the APC-2. In addition, the reflectance of HTPC increases with increasing the incidence angle, which reduces the penetration area of the heating element. The reflections between the tape and the substrate are modelled using a ray-tracing method including the effects of the compaction force on the deformable roller and the tilt  
475 angle of the robot head. It is shown that the reflection occurring between the incoming tape and the substrate increases the laser distribution near nip-point process.

The heat transfer between the substrate and the incoming tape has been investigated using 2D transient finite element models. The non-uniform  
480 laser distribution and inter-layer thermal contact resistance are successfully integrated in thermal models. The numerical model predictions are compared with experimental data obtained from thermocouple measurements during the layup process. A very good agreement is observed. A major point of this model is its ability to describe the temperature at the nip-point process  
485 more precisely at the interface of the PEI film, which is difficult to know by using an IR camera due to the presence of shadow zone between the visible nip-point and nip-point process. Furthermore, the semi-transparent PEI film is heated by conduction and the maximum temperature is located in APC-2 interface emitted by carbon fibres. From the quasi-static model,  
490 an imposed temperature at the nip point process is obtained by iterative simulations in terms of laser power and layup velocity. Finally, the present numerical simulation tool can be easily adapted to model other materials

with other geometries. Thus, this simulation tool can significantly help to better understand the influence of the process parameters on the heating law  
495 for further hybrid materials using AFP process.

## 6. Acknowledgments

The research leading to these results has received funding from the European Union's Horizon 2020 research and innovation programme under Grant Agreement No 723309. The authors wish to thank K. Henry and Y.M.  
500 Corre at CompositIC lab for their valuable helps and fruitful discussions.

## References

- [1] G. Marsh, Automating aerospace composites production with fibre placement, *Reinforced Plastics* 55 (3) (2011) 32–37. doi:10.1016/s0034-3617(11)70075-3.
- 505 [2] D. H.-J. A. Lukaszewicz, C. Ward, K. D. Potter, The engineering aspects of automated prepreg layup: History, present and future, *Composites Part B: Engineering* 43 (3) (2012) 997–1009. doi:10.1016/j.compositesb.2011.12.003.
- [3] S. Pantelakis, K. Tserpes, *Revolutionizing Aircraft Materials and Processes*, Springer International Publishing, 2020. doi:10.1007/978-3-030-35346-9.  
510
- [4] G. Dolo, J. Férec, D. Cartié, Y. Grohens, G. Ausias, Model for thermal degradation of carbon fiber filled poly(ether ether ketone),

- Polymer Degradation and Stability 143 (2017) 20–25. doi:10.1016/  
515 j.polymdegradstab.2017.06.006.
- [5] C. Brecher, M. Emonts, J. Stimpfl, A. Kermer-Meyer, Production of customized hybrid fiber-reinforced thermoplastic composite components using laser-assisted tape placement, in: B. Denkena (Ed.), New Production Technologies in Aerospace Industry, Springer International  
520 Publishing, 2014, pp. 123–129. doi:10.1007/978-3-319-01964-2\_17.
- [6] R. Schledjewski, Thermoplastic tape placement process - in situ consolidation is reachable, *Plastics, Rubber and Composites* 38 (9-10) (2009) 379–386. doi:10.1179/146580109x12540995045804.
- [7] W. J. B. Groupe, Weld strength of laser-assisted tape-placed  
525 thermoplastic composites, Ph.D. thesis, University of Twente, Enschede (2012). doi:10.3990/1.9789036533928.
- [8] Z. Qureshi, T. Swait, R. Scaife, H. M. El-Dessouky, In situ consolidation of thermoplastic prepreg tape using automated tape placement technology: Potential and possibilities, *Composites Part B: Engineering* 66 (2014) 255–267. doi:10.1016/j.compositesb.2014.  
530 05.025.
- [9] C. Stokes-Griffin, P. Compston, A combined optical-thermal model for near-infrared laser heating of thermoplastic composites in an automated tape placement process, *Composites Part A: Applied Science and Manufacturing* 75 (2015) 104–115. doi:10.1016/j.compositesa.  
535 2014.08.006.

- [10] P. M. Schaefer, D. Gierszewski, A. Kollmannsberger, S. Zaremba, K. Drechsler, Analysis and improved process response prediction of laser- assisted automated tape placement with PA-6/carbon tapes using design of experiments and numerical simulations, Composites Part A: Applied Science and Manufacturing 96 (2017) 137–146. doi:10.1016/j.compositesa.2017.02.008.
- [11] S. M. A. Hosseini, I. Baran, M. van Drongelen, R. Akkerman, On the temperature evolution during continuous laser-assisted tape winding of multiple C/PEEK layers: The effect of roller deformation, International Journal of Material Forming (2020). doi:10.1007/s12289-020-01568-7.
- [12] K. Yassin, M. Hojjati, Processing of thermoplastic matrix composites through automated fiber placement and tape laying methods: A review, Journal of Thermoplastic Composite Materials 31 (12) (2018) 1676–1725. doi:10.1177/0892705717738305.
- [13] G. Dolo, Étude expérimentale et modélisation du procédé de placement de fibres avec chauffe laser, Ph.D. thesis, Université Bretagne Sud, Lorient (2017).
- [14] J. Malchus, V. Krause, A. Koesters, D. G. Matthews, A 25kW fiber-coupled diode laser for pumping applications, in: M. S. Zediker (Ed.), High-Power Diode Laser Technology and Applications XII, Vol. 8965, International Society for Optics and Photonics, SPIE, 2014, pp. 62–71. doi:10.1117/12.2039110.

- 560 [15] V. Krause, A. Koesters, H. Koenig, U. Strauss, Brilliant high-power diode lasers based on broad area lasers, in: M. S. Zediker (Ed.), High-Power Diode Laser Technology and Applications VI, Vol. 6876, International Society for Optics and Photonics, SPIE, 2008, pp. 357–369. doi:10.1117/12.761741.
- 565 [16] C. M. Stokes-Griffin, P. Compston, Optical characterisation and modelling for oblique near-infrared laser heating of carbon fibre reinforced thermoplastic composites, Optics and Lasers in Engineering 72 (2015) 1–11. doi:10.1016/j.optlaseng.2015.03.016.
- [17] O. Baho, G. Ausias, Y. Grohens, J. Férec, Simulation of laser heating distribution for a thermoplastic composite: effects of AFP head parameters, The International Journal of Advanced Manufacturing Technology 110 (7) (2020) 2105–2117. doi:10.1007/s00170-020-05876-9.
- 570 [18] A. Kollmannsberger, R. Lichtinger, F. Hohenester, C. Ebel, K. Drechsler, Numerical analysis of the temperature profile during the laser-assisted automated fiber placement of CFRP tapes with thermoplastic matrix, Journal of Thermoplastic Composite Materials 31 (12) (2018) 1563–1586. doi:10.1177/0892705717738304.
- 580 [19] T. Weiler, M. Emonts, L. Wollenburg, H. Janssen, Transient thermal analysis of laser-assisted thermoplastic tape placement at high process speeds by use of analytical solutions, Journal of Thermoplastic Composite Materials 31 (3) (2018) 311–338. doi:10.1177/0892705717697780.

- [20] M. Di Francesco, L. Veldenz, G. Dell'Anno, K. Potter, Heater power control for multi-material, variable speed automated fibre placement, Composites Part A: Applied Science and Manufacturing 101 (2017) 408–421. doi:10.1016/j.compositesa.2017.06.015.
- [21] F. Yang, R. Pitchumani, Healing of thermoplastic polymers at an interface under nonisothermal conditions, Macromolecules 35 (8) (2002) 3213–3224. doi:10.1021/ma010858o.
- [22] L. J. Bastien, J. W. Gillespie, A non-isothermal healing model for strength and toughness of fusion bonded joints of amorphous thermoplastics, Polymer Engineering and Science 31 (24) (1991) 1720–1730. doi:10.1002/pen.760312406.
- [23] V. Iannone, M. Barile, L. Lecce, Automated fabrication of hybrid thermoplastic prepreg material to be processed by in-situ consolidation automated fiber placement process, MATEC Web of Conferences 188 (2018) 01024. doi:10.1051/mateconf/201818801024.
- [24] M. Iannone, Hybrid semicrystalline-amorphous thermoplastic composites for aeronautical applications, Author(s), 2018. doi:10.1063/1.5045900.
- [25] M. Iannone, F. Esposito, A. Cammarano, Thermoplastic matrix composites for aeronautical applications – the amorphous/semi-crystalline blends option, AIP Publishing LLC, 2014. doi:10.1063/1.4876779.

- [26] Á. Alvaredo-Atienza, L. Chen, V. San-Miguel, Á. Ridruejo, J. P. Fernández-Blázquez, Fabrication and characterization of PEEK/PEI multilayer composites, *Polymers* 12 (12) (2020) 2765. doi:10.3390/polym12122765.
- 610 [27] V. Louët, B. Rousseau, S. Le Corre, N. Boyard, X. Tardif, J. Delmas, D. Delaunay, Directional spectral reflectivity measurements of a carbon fibre reinforced composite up to 450°C, *International Journal of Heat and Mass Transfer* 112 (2017) 882–890. doi:10.1016/j.ijheatmasstransfer.2017.04.125.
- 615 [28] V. Le Louët, Étude du comportement thermique de bandes composites pré-imprégnées au cours du procédé de fabrication afp avec chauffage laser, Ph.D. thesis, Université de Nantes, Nantes (2018).
- [29] S. Y. El-Zaiat, Determination of the complex refractive index of a thick slab material from its spectral reflectance and transmittance at normal incidence, *Optik* 124 (2) (2013) 157–161. doi:10.1016/j.ijleo.2011.11.039.
- 620 [30] A. Borghesi, G. Guizzetti, - Graphite (C), in: E. D. Palik (Ed.), *Handbook of Optical Constants of Solids*, Academic Press, 1997, pp. 449–460. doi:10.1016/b978-012544415-6.50060-1.
- 625 [31] M. Born, E. Wolf, *Principles of optics: Electromagnetic theory of propagation, interference and diffraction of light*, Elsevier Science, 2013.
- [32] A. Zaami, I. Baran, T. C. Bor, R. Akkerman, 3D numerical modeling of laser assisted tape winding process of composite pressure vessels

- and pipes—effect of winding angle, mandrel curvature and tape width,  
630 Materials 13 (11) (2020) 2449. doi:10.3390/ma13112449.
- [33] A. Zaami, M. Schäkel, I. Baran, T. C. Bor, H. Janssen, R. Akkerman,  
A fully coupled local and global optical-thermal model for continuous  
adjacent laser-assisted tape winding process of type-IV pressure vessels,  
Journal of Composite Materials (2020) 002199832094459doi:10.1177/  
635 0021998320944598.
- [34] K. L. Johnson, Contact mechanics, Cambridge University Press, 1987.
- [35] A. Jurkiewicz, Y. Pyr´yev, Compression of two rollers in sheet-fed offset  
printing machine, Acta Mechanica et Automatica 5 (4) (2011) 58–61.
- [36] A. Jurkiewicz, M. Pawlikowski, Y. Pyr´yev, Analytical, numerical  
640 and experimental analysis of the relationship between two rollers axes  
distance and the contact zone, International Journal of Mechanical  
Sciences 131-132 (2017) 722–727. doi:10.1016/j.ijmecsci.2017.07.  
030.
- [37] J. Keyes, The McGraw-hill Multimedia Handbook (1994).
- 645 [38] A. Levy, D. Heider, J. Tierney, J. W. Gillespie, Inter-layer thermal  
contact resistance evolution with the degree of intimate contact in the  
processing of thermoplastic composite laminates, Journal of Composite  
Materials 48 (4) (2014) 491–503. doi:10.1177/0021998313476318.
- [39] J. Grünewald, P. Parlevliet, V. Altstädt, Definition of process  
650 parameters for manufacturing of thermoplastic composite sandwiches -

Part A: Modelling, *Journal of Thermoplastic Composite Materials* 31 (6)  
(2018) 745–766. doi:10.1177/0892705717729013.